Soft Matter

ARTICLE TYPE

Cite this: DOI: 00.0000/xxxxxxxxxx

Deformation-dependent polydimethylsiloxane permeability measured using osmotic microactuators[†]

Alexandra R. Spitzer[a] and Shelby B. Hutchens[a,b,*]

Received Date
Accepted Date

DOI: 00.0000/xxxxxxxxxx

In soft solids, large deformations significantly alter molecular structure and device geometry, which can impact other properties. In the case of mass transport, an interplay between flux and mechanical deformation results. Here we demonstrate a platform for the simultaneous characterization of mechano-permselectivity using the (slow) transport of water through polydimethylsiloxane (PDMS) as a challenging test case. The platform uses micron-sized, cylindrical, NaCl solution-filled PDMS chambers encapsulated by selectively-permeable PDMS thin film membranes. When placed in a high chemical potential environment (high water potential) the osmotic pressure difference between the chamber and environment induces water to flow through the PDMS membrane into the chamber, resulting in membrane bulging. A model combining membrane flux and nonlinear elasticity captures the time-dependent response well, but only when a deformation-dependent permeability is used. Notably, the permeability of water through PDMS decreases by nearly an order of magnitude, from 2×10^{-12} to 5×10^{-13} m^2/s, due to primarily to its thickness decreasing by nearly an order of magnitude as the average biaxial stretch increases from 1 to 2.75.

1 Introduction

Membrane permeability determines fluid transport in industrial separations,[1–4] biological function,[5–11] and bio-inspired technologies.[12–19] Frequently, permeability is quantified under rigid, static conditions. However, in soft biological materials and bio-inspired devices, large changes in geometry and/or stretch occur, leading to an interplay between fluid transport and mechanical response that can be central to function. Observations and models of materials'[20–22] and tissues'[23–25] poroelastic response abound in hydrated and porous materials, for which transport is governed by Darcy's law. Yet few methods to measure the mechano-transport properties in materials exhibiting a solution-diffusion mechanism have been reported.[26–29] Here, we demonstrate a small-scale, bulge-based test platform for quantifying membrane mechano-permselectivity. Using this approach, we evaluate the deformation-dependent permeability of water within commercial polydimethylsiloxane (PDMS), an elastomer known for its biocompatibility and high stretchability as well as its separations properties (*e.g.*, pervaporation[30]). This small-scale approach resolves small flux volumes, which are particularly challenging to measure in membranes with extremely low permeability, including water through PDMS.

Previous investigations of water permeability within PDMS find that it is low and dependent on network structure, but its deformation or geometry-dependence has not been described. However, for gas and vapor permeants (CO_2, H_2, and H_2O), PDMS reportedly becomes *thickness* dependent below tens of microns.[31,32] The behavior is attributed to non-equilibrium sorption-desorption processes at the interface, which take over as the dominant flux-limiting mechanism for sufficiently thin films.[33]

A membrane's microstructure can also regulate its permeability[34] via structural contributions to both the sorption of a solution *into* the membrane and subsequent diffusivity *within* it.[35,36] Under load, polymeric membranes experience deformation that modifies that microstructure. Consistent with other polymeric membrane systems,[27,37,38] PDMS's permeability to water vapor has been found to decrease as the chain mobility decreases;[29] mobility was controlled by changing crosslink density and verified with its proportionality to the glass transition temperature. Notably, Song, et al.[39] reported stretch dependent permeability of *ethanol* through PDMS. However, the mechanism used to capture the response derives from changes in hydraulic resistance to flow within channels in the network. Such channels are possible for ethanol, since ethanol slightly swells PDMS by 4%.[40] However, PDMS is known to be highly hydrophobic, exhibiting swelling of

---

[a] Department of Materials Science and Engineering, University of Illinois Urbana-Champaign, Urbana, IL, USA.
[b] Department of Mechanical Science and Engineering, University of Illinois Urbana-Champaign, Urbana, IL, USA. E-mail: hutchs@illinois.edu; Tel: +1 (217)300-0412

[†] Electronic Supplementary Information (ESI) available: : Nine pages of supplementary text and figures. See DOI: 10.1039/cXsm00000x/

Accepted Version: accepted Jul 19, 2023

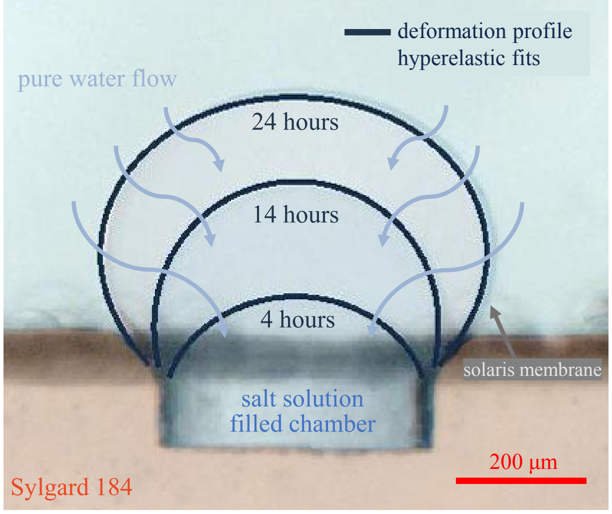

Fig. 1 Overlayed, time-lapse optical images of a bulging membrane in cross-section at 4, 14, and 24 h. Dark blue curves are deformation profile *fits* of a nonlinear bulge model employing the Gent 3-parameter strain energy density function.

$\sim 0.1\%$,[41] which could *at most* yield submicron channels that would deviate from typical hydraulic behavior. The results we present here suggest a potentially minor effect of material stretch on permeability for this PDMS system and a description of stretch-dependent permeability in non-swelling network solids is outside the scope of the current work.

Our experimental design employs an osmolyte-filled chamber and a deformable, selectively permeable membrane that bulges as fluid enters (Fig. 1). Modeling chamber dynamics necessitates combining 1) membrane-mediated, osmosis-driven flow, 2) variable membrane surface area and thickness (in contrast to devices that separate actuation and permeability functions) and 3) nonlinear mechanical constitutive behavior.[42–46] Our approach to these requirements combines the following previous work. In describing the capabilities of osmotic actuators, Sinibaldi et. al.[13,14] modeled the volumetric actuation, characteristic actuation time, maximum applied force, and peak power of a bulging membrane under the assumption of *linear* elasticity attached to a large, *rigid*, osmotically-active chamber (fixed permeable surface area and thickness). The device is theoretically reversible.[47] We modify their framework to achieve the second point above by predicting chamber geometry changes via nonlinear membrane mechanics (third point). Experimental characterization of the deformation of pressurized hyperelastic membranes has been successfully captured by both analytical[48–50] and finite-element models.[51,52] Interestingly, while bulge deformation profiles are reported, model validation typically compares pressure to a single parameter, applied fluid volume[48] or maximum membrane displacement.[49,51,52] Here we show agreement between the hyperelastic membrane model[53] and the *entire bulge profile*, strengthening the flux model fidelity and therefore the argument for a varying permeability during actuation.

The article is organized as follows. First, we describe the materials and methods. Next, we discuss the principles driving chamber operation. Membrane mechanics comprise a key input of the modeling framework, and we provide solutions for both linear elastic and hyperelastic materials. Finally, the model is compared with the experimental time-dependent response. As a proof-of-concept, we report on the effects of incorporating hydrophilic components within the PDMS membrane to increase its sorption coefficient and therefore permeability.

2 Materials and Methods

Using a soft lithography approach, we form NaCl-filled chambers encapsulated by thin PDMS films.

2.1 Materials

We use two commercially available PDMS formulations (Sylgard 184, Solaris) and one PDMS-based composite (PEO-Solaris).

Sylgard 184, cylindrical chamber base. Sylgard 184 (Dow Corning) in a 10:1 (wt:wt) ratio, prepolymer base to curing agent is mixed for 45 s at 2500 RPM in a SpeedMixer (Flactek, Inc.)

PDMS (Solaris), membranes. Solaris (Smooth-On, Inc.) parts A and B are mixed in a 1:1 (wt:wt) ratio for 45 s at 2500 RPM in the SpeedMixer.

PEO-PDMS (Solaris), membranes. PDMS composite membranes are composed of allyloxy polyethylene oxide (PEO) (GELEST, INC.) and Solaris. Following previous work,[54] a 10:1 (wt:wt) dichloromethane (DCM) (Fisher) to polyethylene oxide (PEO) (GELEST, INC.) solution is hand mixed for 1 min. DCM-PEO is added to uncured Solaris at a ratio of 1.25 g of DCM-PEO per 25 g Solaris (5000 ppm (by mass) PEO), mixed for 45 s, at 2500 RPM (SpeedMixer), then degassed in a vacuum chamber.

2.2 Device Fabrication

Cylindrical well-structures in Sylgard 184 are immersed in NaCl solution. Elastomeric membranes consisting of a cured/uncured bilayer are adhered to the immersed structures, thereby encapsulating solution within the chambers.

PDMS Chamber Fabrication. Sylgard 184 chambers are molded (30 min degas; 70°C cure; 1.5 h) from a photolithographically patterned[55] micropillar mold. The mold is comprised KMPR 1010 negative photoresist (Microchem) micropillars of radii ranging from 100-200 μm and a height of 110 μm.

Selectively Permeable Membrane Fabrication. Solaris and PEO-Solaris membranes are spun coat (Laurell Technologies) on glass slides. First, polyacrylic acid (PAA) (Sigma Aldrich) and reverse osmosis (RO) water solutions (Table 1) are deposited at 1000 RPM for 40 s, to serve as a sacrificial layer. Films are placed on a hotplate at 100°C for 1 min to cure and eliminate excess water. Then PDMS is deposited twice; the first layer is cured (70°C for 1 h) and the second left uncured to serve as an adherent. Each layer is spun for 5 min according to the information in Table 1.

Structure Assembly. We test 5 or more devices for each of the following experimental configurations: reference chamber ($a = 200\ \mu$m, $l_0 = 20\ \mu$m, $h = 110\ \mu$m, and $C_0 = 3$ M), small radius chamber ($a = 100\ \mu$m), thick membrane chamber ($l_0 = 26\ \mu$m), reduced osmotic loading chamber ($C_0 = 1$ M), and PEO-PDMS membrane chamber ($a = 200\ \mu$m, $l_0 = 20\ \mu$m,

Table 1 Selectively-permeable Membrane Spin Coating Process Conditions

Membrane	PAA Solution (wt.%)	Cured Layer Speed (RPM)	Adherent Layer Speed (RPM)	Membrane Thickness (μm)
Solaris	5	3000	2500	20
Solaris	5	2000	2000	26
PEO-Solaris	15	3000	2500	20

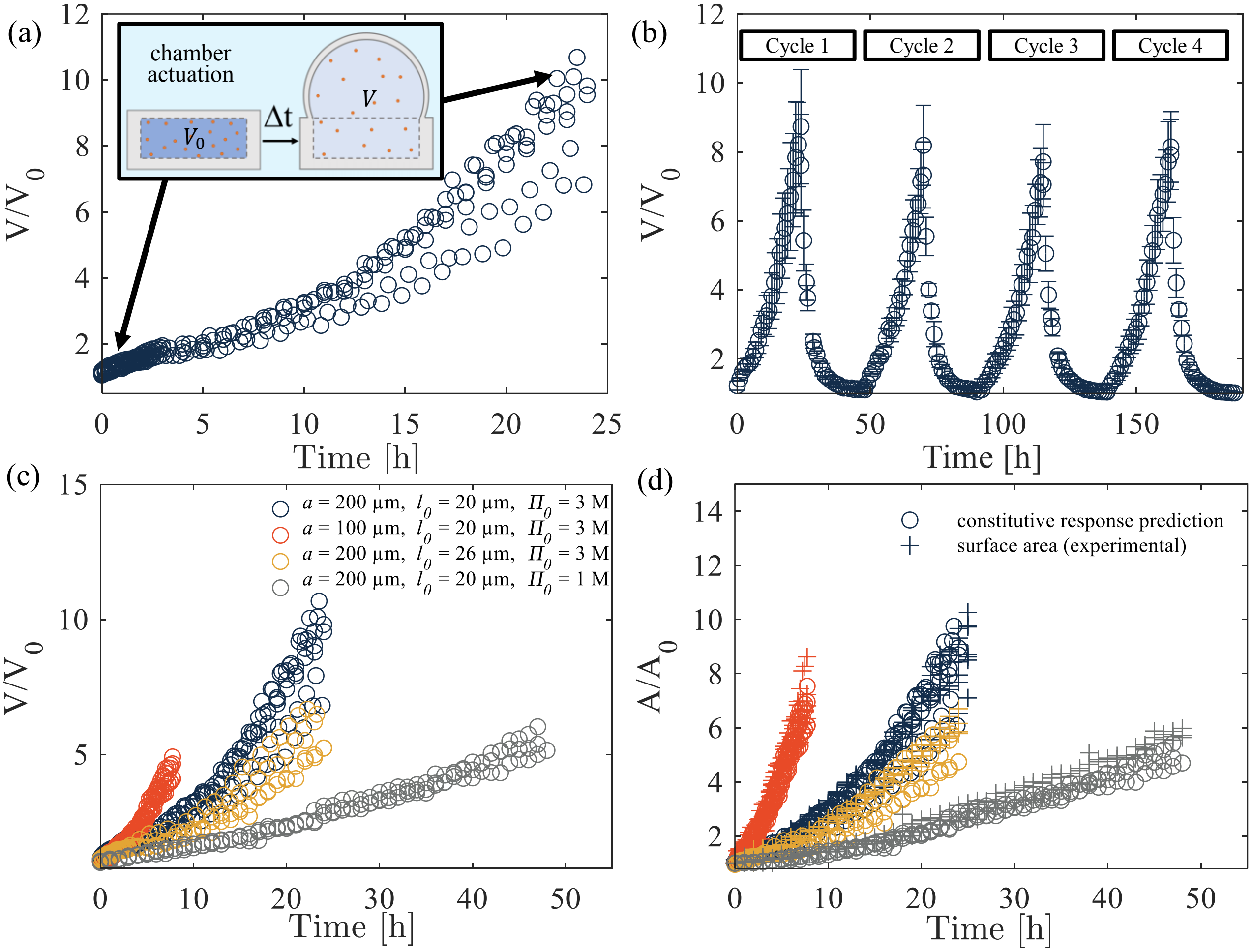

Fig. 2 Normalized actuation response of microchambers over time. (a) The normalized volume V/V_0 of the reference chamber ($a =$ 200 μm, $l_0 =$ 20 μm, $C_0 =$ 3 M) exhibits a nonlinear time-dependent response (7 samples). (b) Reversible reference chamber actuation across 4, 48 h cycles indicate negligible salt leakage over this time scale. (c) Four actuation chamber conditions are investigated in this work: the reference conditions (navy blue, same as (a)), a small radius chamber: $a =$ 100 μm (orange), a thick membrane chamber: $l_0 =$ 26 μm (gold), and a reduced osmotic loading chamber: $C_0 =$ 1 M (gray). (Unlisted parameters match the reference.) (d) Actuation response expressed as membrane surface area ratio $\frac{A}{A_0}$ over time is equivalent to V/V_0. For the four actuation chamber conditions in (c), direct experimental measurement (crosses) and conversion from V/V_0 (as plotted in (c)) using the mechanical bulge model (circles) provide similar results.

$h =$ 110 μm, and $C_0 =$ 3 M) where unspecified conditions match the reference chamber. Before assembly, the NaCl solution (3 or 1 M solutions in RO water) is degassed for 30 min to pull water into the wells. Membrane assemblies are fixed to a test stand mounted (TA.XT Plus 100, StableMicrosystems) cylindrical compression probe and brought into contact with the submerged chambers at a rate of 1 mm/min to a pressure of 50 kPa. The structure is held in compression for 12 h, curing the adherent layer and dissolving the PAA layer.

2.3 Imaging and Analysis

Optical micrographs of the device cross-section (Fig. 1) are taken every 10-15 min over a span of 24 h (AxioObserver, Zeiss). Custom MATLAB code fits an elliptical curve to each membrane deformation profile from which volume change is determined via integration.

2.4 Mechanical Characterization

We characterize mechanical response by simultaneously fitting the bulge geometry in the previous section and a standard uniaxial test geometry.

Uniaxial Tension. We fabricate tensile specimens with 'dogbone' geometries (ASTM D412-16, die type D) and load them at a strain rate of 0.03 s^{-1}, using optical strain quantification (fiducial markers) until rupture (5 kg load cell).

3 Results and Discussion

The following results demonstrate the necessity of a deformation-dependent PDMS water permeability, arising from the inability of a time-dependent flux model with *constant permeability* to accurately capture experimentally-observed chamber volume evolution. This shortcoming occurs despite accurate accounting of finite deformation mechanics in the microactuator's response.

3.1 Bulging of Osmotically-Active Chambers

Driven by an osmotic pressure difference, pure water in the environment permeates the thin membrane into the salt-water-filled chambers, deflecting the membrane to accomodate the increased chamber volume (Fig. 1). Mechanical equilibrium requires that the hydrostatic pressure within the chamber increase to support the bulging membrane. The increase in hydrostatic pressure P_t and the decreased magnitude of the osmotic potential Π ($\Pi < 0$ for finite salt concentration) combine to increase the chamber water potential Ψ. Ψ quantifies the driving force for water movement, where water flows from regions of high to low potential. For pure water at atmospheric pressure, $\Psi = 0$ (ESI[†]). We calculate the total volume of water in the chamber V from the bulged profile assuming cylindrical symmetry. Fig. 2a illustrates the normalized time-dependent evolution of the chamber volume V/V_0 for a set of chambers in what we refer to as the reference configuration (chamber radius $a =$ 200 μm, initial membrane thickness $l_0 =$ 20 μm, chamber height $h =$ 110 μm, and initial salt concentration $C_0 =$ 3 M). This data was gathered to the point at which observation was hindered by: membrane delamination, membrane fracture, or interference between bulges. Despite slow permeability in silicone membranes, volume increases by a factor of 8 over 24 h due to the actuator's small size.

Two key benefits accompany the day-length timescale of actuation. First, within the microscale chamber, both solute and solvent diffuse across the entire chamber within approximately 3 s (ESI[†]). This separation of local mixing and macroscopic deformation time scales means the chamber can be considered well-mixed and concentration polarization does not occur. Additionally, the process is quasi-static, thus we ignore viscoelastic effects. These features provide the basis for many of the assumptions used in the model to follow.

The membrane bulges due to water flow through the membrane, so it is possible the osmolyte could permeate, resulting in salt leakage. To quantify salt-leakage, we actuate these membranes through four cycles. Forward actuation (bulging) is induced by submerging devices in pure RO water, causing water to flow through the membrane in a response to the lower water potential inside the chamber. After 24 h of forward actuation, the feed solution is replaced with a solution isotonic to the initial chamber solution and reverse actuation commences for 24 h due to a reversal of water potential. As Fig. 2b shows, observations across four cycles reveal no significant difference in maximum actuation, unactuated state, or time-scale of actuation. With these results as motivation, we make the assumption that on the time-scale of these studies, no significant salt leakage occurs.

Qualitatively, variations in actuator parameters yield anticipated trends. As shown in Fig. 2c, a smaller chamber radius a increases the rate at which actuation occurs (increased V/V_0 vs. t slope, orange) and a thicker membrane l_0 and lower initial salt concentration C_0 decrease the rate at which it occurs (gold and gray data, respectively). (All chambers have the same 110 μm depth.) We validate the model developed in the following section by quantitatively capturing all of these responses using a single permeability function.

The membrane area and thickness increase and decrease, respectively, as the actuator volume increases. We track and model chamber volume in this work, however, one might equivalently measure membrane area evolution as a function of time. In Fig. 2d (plus signs) we illustrate the time evolution of the normalized membrane surface area A/A_0, where A and A_0 are the instantaneous and initial membrane area, respectively. These data arise from a surface integral (assuming cylindrical symmetry) of the experimental bulge profile. Using the hyperelastic bulge model developed in Sec. 3.4 reproduces the area response (Fig. 2d, circles) for a series of experimentally determined V/V_0 values from the same conditions Fig. 2c , thereby illustrating the invariance of the results with respect to the chosen observable.

Interestingly, at sufficiently large deformation, the region surrounding the peak of the bulge begins to exhibit color variations, possibly due to interactions with visible light (ESI[†], Fig. S11). Predictions of film thickness at an experimentally determined $A/A_0 \sim 12 - 13.5$ suggest the center of the film is on the order of 800-900 nm, just above the wavelength of visible light. We leave this observation for future exploration.

3.2 Modeling Volumetric Flow Rate and Permeability

In this section, we develop the first order differential equation describing chamber volume time evolution for arbitrary membrane mechanics. Assumptions include: water potential defined relative to pure water at atmospheric pressure, negligible salt leakage from an ideal solution enclosed in the chamber, and first order Fickian diffusion through the membrane.

3.2.1 Flux Through a Membrane.

Water passes through a silicone membrane via solution-diffusion,[56] meaning that molecules must first dissolve from a reservoir into the membrane and then release from the other side after passing through. Within the membrane, the water obeys Fick's first law, resulting in a linear dependence of volumetric flux J_Q on the driving force across the membrane due to water potential Ψ. Ψ is the sum of the osmotic potential Π and turgor pressure P_t, with $\Pi = -iCRT$ (Van't hoff's law) and $P_t = 0$ at atmospheric pressure. (The solute electronic dissociation factor, solute concentration, universal gas constant, and temperature are represented by i, C, R, and T, respectively.) Thus, volumetric flux [units: $\mathrm{m}^3/(\mathrm{m}^2\mathrm{s})$] is given by

$$J_Q \propto -\nabla\Psi = -L\frac{(\Pi+P_t)}{l} \tag{1}$$

where the potential gradient is applied over a film of thickness l and the pure reservoir reference state ($\Psi = 0$) is implicitly accounted for. L is the constant of proportionality that mediates the potential gradient and in this case is the mobility, which is given by (see ESI†)

$$L = \frac{P_w C_\mathrm{W}}{RT}\frac{V_m M_w}{\rho_w}, \tag{2}$$

and defined in terms of the membrane's permeability to water P_w; the solution water concentration C_w; and the molar volume, molecular weight, and mass density of water V_m, M_w, and ρ_w. Permeability includes both solution into and out of the membrane and the diffusive behavior through the membrane and thus is further decomposed into

$$P_w = D_w \cdot K_{\mathrm{w:membrane}} \tag{3}$$

where $K_{\mathrm{w:membrane}}$ defines the sorption or partition coefficient between the reservoir and the membrane [unitless] and D_w is the diffusivity of the water within the membrane [units: m^2/s].

3.2.2 Chamber Volume Evolution

We assume that deflection of the thin membrane encloses a volume ΔV equal to the volume of the water that enters due to fluid incompressibility and negligible deflection of the stiffer, thicker chamber walls. It is convenient to track membrane deformation independent of initial-chamber-geometry using a dimensionless, deflected membrane volume $\tilde{V}$

$$\tilde{V} = \frac{\Delta V}{A_0 a} = \frac{V - V_0}{A_0 a} = \frac{\frac{V}{V_0} - 1}{\frac{A_0 a}{V_0}} \tag{4}$$

as chamber turgor pressure, membrane thickness, and membrane area vary naturally with $\tilde{V}$ according to the membrane's constitutive behavior only (rather than V_0). The instantaneous rate of change in chamber volume $\frac{dV}{dt}$ due to volumetric water flux J_Q is therefore

$$\frac{dV}{dt} = \iint\limits_{A(\tilde{V})} J_Q(\tilde{V}) \;\; dS \tag{5}$$

where $A(\tilde{V})$ denotes the area of the surface S over which $\tilde{V}$-dependent flux is integrated. Eqn. (1) illustrates that J_Q's dependence on $\tilde{V}$ arises via Π, P_t, and l. The first two terms, Π and P_t are uniform within the chamber due to its being well-mixed and under hydrostatic pressure, respectively. The potential for flow due to osmotic pressure decreases as a function of the increasing chamber volume, $\Pi = \Pi_0 \frac{V_0}{V}$, where $\Pi_0 = -iC_0RT$ and C_0 is the initial osmolyte concentration. P_t's dependence on $\tilde{V}$ will be addressed in Sections 3.3 and 3.4. The film thickness l varies across the deformed surface and in general cannot be treated as an average value (ESI†). The time-dependent chamber volume change therefore becomes

$$\frac{dV}{dt} = -L\left(\Pi_0\left(\tfrac{V_0}{V}\right) + P_t(\tilde{V})\right) \iint\limits_{A(\tilde{V})} \frac{1}{l(\tilde{V})} \;\; dS \tag{6}$$

We recognize the integral term as being $A\langle 1/l\rangle$ (where $\langle\cdot\rangle$ denotes the expectation value). Substituting this relation and nondimensionalizing Eqn. (6) for all variables except time, yields

$$\frac{d\frac{V}{V_0}}{dt} = -\frac{L\Pi_0 A_0}{l_0 V_0}\frac{A(\tilde{V})}{A_0}\left\langle \frac{l_0}{l(\tilde{V})}\right\rangle \left(\frac{1}{\frac{V}{V_0}} + \frac{P_t(\tilde{V})}{\Pi_0}\right) \tag{7}$$

which motivates the definition of three dimensionless expressions characterizing membrane deflection mechanics: $f_A(\tilde{V}) = \frac{A(\tilde{V})}{A_0}$, $f_l(\tilde{V}) = \left\langle \frac{l_0}{l(\tilde{V})}\right\rangle$, and $f_p(\tilde{V}) = \frac{P_t(\tilde{V})}{E}$. (We use Young's modulus E to nondimensionalize turgor pressure P_t.) Re-writing Eqn. (7) with these functions gives the final result for the time-dependent, instantaneous dimensionless volume change of the actuating chamber

$$\frac{d\frac{V}{V_0}}{dt} = -\frac{L\Pi_0 A_0}{l_0 V_0} f_A(\tilde{V}) f_l(\tilde{V}) \left(\frac{1}{\frac{V}{V_0}} + \frac{E f_p(\tilde{V})}{\Pi_0}\right), \tag{8}$$

where $\tilde{V}$ and V/V_0 are related according to Eqn. (4). This form suggests that an appropriate time constant for the system is:

$$\tau = -\frac{l_0 V_0}{L\Pi_0 A_0}. \tag{9}$$

For a given mechanical response (f_A, f_l, and f_p) and water mobility L within the membrane, Eqn. (8) predicts the dimensionless time-dependent response of an actuating chamber as

$$\frac{d\frac{V}{V_0}}{d\tilde{t}} = f_A(\tilde{V}) f_l(\tilde{V}) \left(\frac{1}{\frac{V}{V_0}} + \frac{E f_p(\tilde{V})}{\Pi_0}\right). \tag{10}$$

3.3 Linear Elastic Membrane Bulge Theory

Assuming linear elasticity as a simple starting point provides some insight into the dimensionless functions' f_A, f_l, and f_p dependence on $\tilde{V}$. As we will show, this small strain assumption is poor for most of the observed deformation and in the next section, we provide the more complex, hyperelastic description.

An expression for chamber turgor pressure arises from the combination of Timoshenko's linear elastic cylindrical membrane bulge theory[57] and the Nix approximation[58] connecting the deflection distance to the deflected volume using. Using a spherical cap approximation provides a reasonable estimate of the deflected membrane's surface area for a given deflection distance.[13] Combined with an assumption that under small deformation, the membrane exhibits negligible changes in thickness, these relations yield the following expressions (See ESI† for details):

$$f_p(\tilde{V}) = \frac{P_t(t)}{E} = \frac{128\pi^2}{3}\frac{l_0}{A_0^5}(V(t) - V_0)^3 = \frac{128}{3}\frac{l_0}{a}\frac{\tilde{V}^3}{} \tag{11}$$

$$f_A(\tilde{V}) = \frac{A(t)}{A_0} = 1 + \frac{4(V(t) - V_0)^2}{a^4} = 1 + 4\pi\tilde{V}^2 \tag{12}$$

$$f_l(\tilde{V}) = \frac{l_0}{l(\tilde{V})} = \frac{l_0}{l_0} = 1 \tag{13}$$

Shown gold lines in Fig. 3 a, b, and c, the linear approximation predicts an overly stiff membrane response with volume change, only agreeing with the hyperelastic response at the lowest values

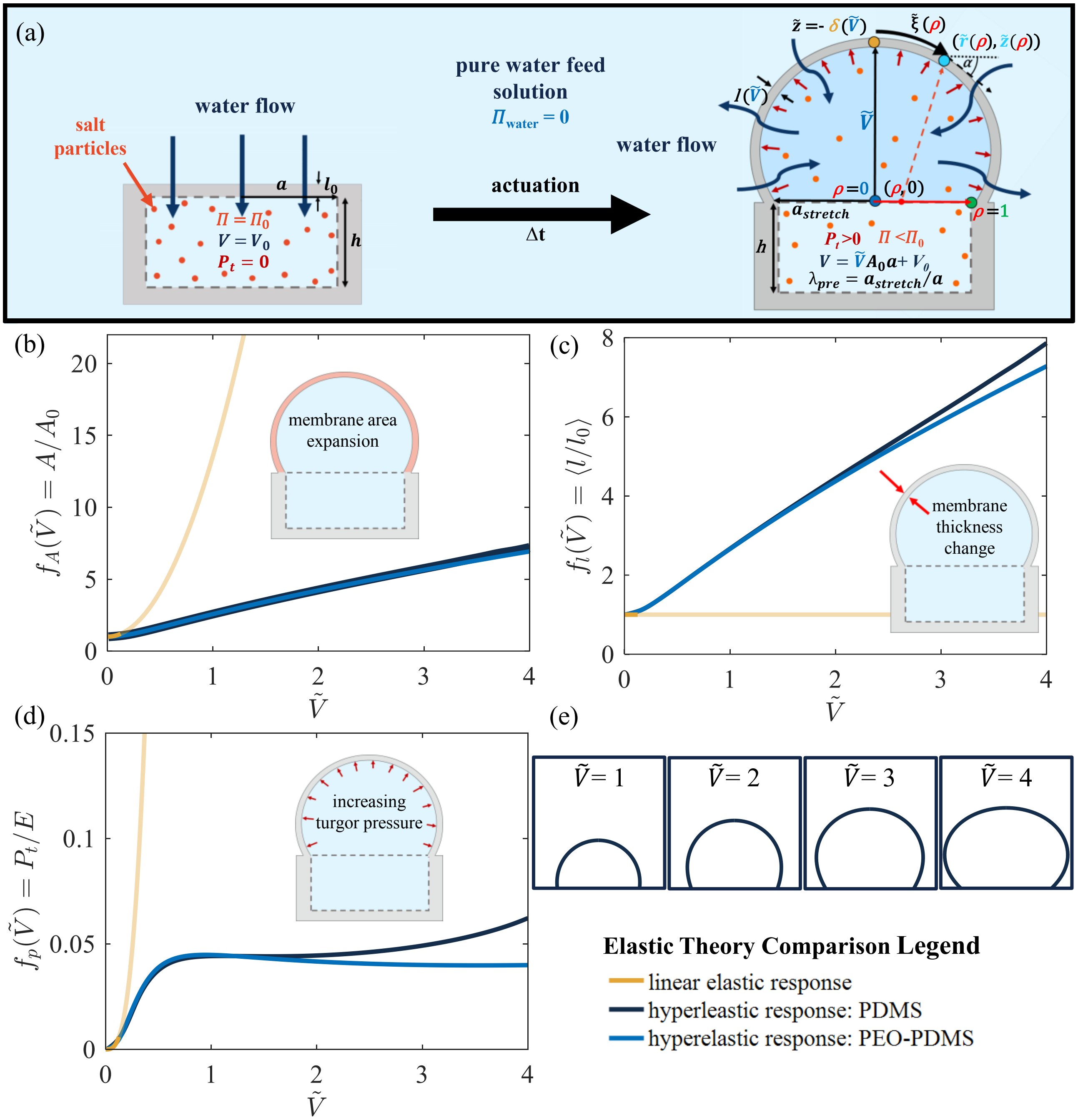

Fig. 3 Mechanical model of bulging membrane. (a) Water enters the chamber through the selectively permeable membrane, driven by the initial osmotic pressure Π_0. The membrane deflects along the -$\tilde{z}$-axis to a maximum of $-\delta$ while developing turgor pressure P_t. Equilibrium membrane geometry is parameterized by ρ, the initial radial position in the undeformed configuration which stretches to a dimensionless arc length $\tilde{\xi}(\rho)$ for deformed coordinates $\tilde{r}(\rho)$ and $\tilde{z}(\rho)$. For reference chamber conditions, three dimensionless functions characterize the bulged membrane area (b), inverse thickness (c), and turgor pressure (d) as a function of dimensionless bulge volume $\tilde{V}$. Three constitutive responses are shown: linear elastic with an equivalent modulus (gold; light gold beyond the small stretch regime), hyperelastic PDMS (navy), and hyperelastic PEO-PDMS (light blue). (Hyperelasticity details in Sec. 3.4.) (e) The bulge deformation profile of a hyperelastic PDMS membrane in the reference geometry illustrates the shape evolution across $\tilde{V} = (0,4)$. All curves set $\lambda_{pre} = 1$.

of deflection, $\tilde{V} < 0.05$ (saturated gold region). This level of deflection corresponds approximately to an average biaxial stretch within the membrane of $\overline{\lambda} = \sqrt{A/A_0} \sim 1.2$.

3.4 Hyperelastic Membrane Mechanics

To capture large membrane deformation, we use a hyperelastic bulge model[53,59] to define $f_A(\tilde{V})$, $f_l(\tilde{V})$, and $f_p(\tilde{V})$. We treat the membrane as an incompressible Gent 3-parameter material[60] with strain energy density function,

$$W = -C_1 J_m \ln\left(1 - \frac{J_1}{J_m}\right) + C_2 \ln\left(\frac{J_2+3}{3}\right), \tag{14}$$

expressed in terms of the first and second strain invariants J_1 and J_2, defined as

$$J_1 = \lambda_\xi^2 + \lambda\phi^2 + \frac{1}{\lambda_\xi \lambda\phi}^2 - 3, \tag{15}$$

$$J_2 = \lambda_\xi^{-2} + \lambda\phi^{-2} + \frac{1}{\lambda_\xi \lambda\phi}^{-2} - 3. \tag{16}$$

This model captures the mechanical response of the membrane materials using parameters fit from both mechanical characterization geometries. Uniaxial tensile data are available in the ESI†. The resulting fit parameters, combined with the following equations, capture the experimentally observed deformation (Fig. 1, dark-blue lines).

3.4.1 Deformed Membrane Profile.

We determine the membrane deformation profile guided by the work of Long, *et al.*[53] who combine governing equations describing the deformation of a hyperelastic cylindrical cap[59] with clamped boundary conditions at the cylinder edge. Throughout, we use their definitions for parameters, but nondimensionalized with respect to length using the initial membrane radius a (*e.g.*, $\tilde{r} = r/a$, $\tilde{z} = z/a$). These variables are illustrated in Fig. 3a. The membrane is parameterized using ρ, $0 \le \rho \le 1$, with the undeformed radial membrane profile lying along the $\tilde{r}$-axis at $\tilde{z} = 0$ from $\rho = 0$ at $\tilde{r} = 0$ to $\rho = 1$ at $\tilde{r} = 1$. The deformed membrane coordinates are expressed as functions the parameter ρ as ($\tilde{r}(\rho)$, $\tilde{z}(\rho)$). Each position on the deformed profile is associated with an arc-length $\tilde{\xi}(\rho)$, where the initial point $\tilde{\xi}(\rho) = 0$ occurs at $\rho = 0$. The angle formed by the tangent line to each deformed point is $\alpha(\rho)$. In the deformed state, the membrane experiences principal stretch ratios $\lambda_\xi(\rho)$, $\lambda_\phi(\rho)$, and $\lambda_r(\rho)$ at each position ρ. The longitudinal and latitudinal stretches are defined, respectively, as

$$\lambda_\xi(\rho) = \frac{d\tilde{\xi}}{d\rho} \qquad \lambda_\phi(\rho) = \frac{\tilde{r}}{\rho}, \tag{17}$$

and the assumption of membrane incompressibility requires $\lambda_r(\rho)$, the stretch ratio related to the dimensionless change in membrane thickness, to be:

$$\lambda_r(\rho) = \frac{1}{\lambda_\xi(\rho)\lambda_\phi(\rho)} = \frac{l(\rho)}{l_0}. \tag{18}$$

In an ideal system, changes in P_t deform only the membrane. However, experimentally we observe expansion of the compliant PDMS chamber with increasing P_t (corresponding to increasing $\tilde{V}$). We account for this effect using as an experimentally measured radial membrane pre-stretch, $\lambda_{\mathrm{pre}}(\tilde{V})$ (ESI† Fig. S6).

Boundary conditions capture 1) the fixed $\tilde{z}$ of the membrane edge, 2) the stretch ratio at the fixed edge (equal to λ_{pre}), 3) a constant encapsulated bulge volume, and 4) an assumption of radial symmetry. These are expressed as

$$\tilde{z}(\rho = 1) = 0$$

$$\lambda_\phi(\rho = 1) = \lambda_{pre}$$

$$\tilde{V}(\rho = 0) = 0 \qquad \tilde{V}(\rho = 1) = \tilde{V}$$

$$\lambda_\xi(\rho = 0) = \lambda_\phi(\rho = 0) \qquad \alpha(\rho = 0) = 0$$

respectively, where the latter reflect the equibiaxial extension and horizontal tangent line at the membrane's center. These boundary conditions limit solutions to physically-relevant deformation profiles for a given turgor pressure. We found that fixed bulge volume was critical to modeling strain stiffening materials, as opposed to fixed deflection at $\tilde{z} = 0$, because the latter does not provide a unique solution as the bulge begins to flatten at large deformations.

Labai and Simmonds[59] derived the static equilibrium and geometric relationships to describe membrane deformation under the application of uniform pressure P_t. For the Gent 3-parameter constitutive model, the natural nondimensionalization of the turgor pressure is $\tilde{P}_t = \frac{P_t a}{C_1 l_0}$. Using this dimensionless parameterization, Labai and Simmonds equations, and a differential form for determining the volume $\tilde{V}$ from the membrane profile (a function of ρ, λ_ϕ, and $\tilde{z}$), we define 5 governing equations,

$$\frac{d\lambda_\xi}{d\rho} = \frac{\lambda_\xi(\tilde{T}_\phi - \tilde{T}_\xi)\cos\alpha - \lambda_\phi \frac{\partial \tilde{T}_\xi}{\partial \lambda_\phi}(\lambda_\xi \cos\alpha - \lambda_\phi)}{\rho \lambda_\phi \frac{\partial \tilde{T}_\xi}{\partial \lambda_\xi}} \tag{19}$$

$$\frac{d\alpha}{d\rho} = \frac{\tilde{P}_t \rho \lambda_\phi \lambda_\xi - \lambda_\xi \tilde{T}_\phi \sin\alpha}{\rho \lambda_\phi \tilde{T}_\xi} \tag{20}$$

$$\frac{d\lambda_\phi}{d\rho} = \frac{\lambda_\xi \cos\alpha - \lambda_\phi}{\rho} \tag{21}$$

$$\frac{d\tilde{z}}{d\rho} = \lambda_\xi \sin\alpha \tag{22}$$

$$\frac{d\tilde{V}}{d\rho} = \lambda_\phi \rho^2 \frac{d\tilde{z}}{d\rho} \tag{23}$$

where the dimensionless line tensions in the ξ and ϕ directions are given as derivatives of the strain energy density function W, and nondimensionalized by the Gent-parameter, C_1:

$$\tilde{T}_\xi = \frac{1}{C_1 \lambda_\phi} \frac{\partial W}{\partial \lambda_\xi} \qquad \tilde{T}_\phi = \frac{1}{C_1 \lambda_\xi} \frac{\partial W}{\partial \lambda_\phi}. \tag{24}$$

We solve this set of ordinary differential equations (ODEs) by integrating over $0 \le \rho \le 1$ and enforcing the described boundary conditions, using the MATLAB boundary value solver BVP5C. For a given deformed volume $\tilde{V}$, we solve for the dimensionless pressure $\tilde{P}_t$ required to deform the membrane and the parameters defining the membrane geometry $\lambda_\xi(\rho)$, $\alpha(\rho)$, $\lambda_\phi(\rho)$, $\tilde{z}(\rho)$, and $\tilde{V}(\rho)$ for $0 \le \rho \le 1$. The initial guess is a spherical cap approximating the pressure with that of neoHookean membrane of similar volume.[53] The solution maps to the deformation profile

$(\tilde{r}(\rho), \tilde{z}(\rho))$ via the functions $\tilde{z}(\rho)$ and $\lambda_\phi(\rho)$ with the relation to $\tilde{r}$ given by Eqn. (17). A series of profiles are shown in Fig. 3e.

3.5 From Profile to Membrane Geometry

Each membrane profile corresponds to a unique turgor pressure P_t. Thus, the deformed geometry, as parameterized by the dimensionless volume enclosed by the deflecting membrane $\tilde{V}$, can be linked to P_t, l, and A to define the hyperelastic membrane mechanics functions $f_A(\tilde{V})$, $f_l(\tilde{V})$, and $f_p(\tilde{V})$ required to fully define Eqn. (8). For each 'turgor pressure' - 'deformed profile' pair, we verify the volume enclosed by the membrane profile and calculate the membrane surface area and the average inverse thickness via integration. (See ESI† for details.) For f_l, average inverse thickness is nearly equivalent to the inverse of the average membrane thickness for the constitutive response and loading conditions here (ESI Fig. S1).

Figure 3 provides $\tilde{V}$ dependence for membranes well beyond a hemispherical cap, $\tilde{V} = 2/3$. We include predictions for experimentally-determined constitutive responses from the two material systems considered here: Solaris (navy lines) and PEO-Solaris (light blue lines). For devices such as those we report here, in which the bulging surface serves as *both* actuator and membrane, nearly order-of-magnitude increases in membrane area and inverse thickness (decreased thickness) critically mediate the volumetric flux (Eqn. (8)) for a given driving force $(\Pi + P_t)/\Pi_0$. Pressure, on the other hand increases slowly (or plateaus in the case of PEO-PDMS) meaning that for thin, highly deformable films the evolution of the driving force for flow is primarily mediated by changes in osmotic pressure Π/Π_0, which decreases as $\sim V_0/V = \frac{1}{\tilde{V}\frac{A_0 a}{V_0}+1}$.

The complex nonlinearity of this system therefore arises from both the nonlinear material response and the inherent nonlinearity of the ODE. This presents a challenge to easily understanding how the time-dependent response evolves with changes in chamber/membrane geometry or initial osmotic pressure. As an example, we model the volume evolution using *dimensionless* time (Eqn. (9)) assuming constant $P_w = 2 \times 10^{-12}$ m^2/s (Fig. 4a) for the experimental conditions in Fig. 2c. The time-dependent response of a reference chamber ($a = 200$ μm, $l_0 = 20$ μm, $C_0 = 3$ M; navy line) is compared to a smaller radius chamber ($a = 100$ μm; orange line), a membrane with larger initial thickness ($l_0 = 26$ μm; gold line), and a chamber containing a lower initial salt concentration or osmotic potential ($C_0 = 1$ M; gray line). Note that in dimensionless time, the reference, thick membrane, and reduced osmotic pressure curves collapse since 1) these variables are accounted for in the definition of $\tilde{t}$ or 2) in the case of the thick membrane, the thickness change is small enough to produce little variation in f_A, f_l, and f_p. Fig. 4b shows that in the case of the small chamber the faster relative response time arises from increased geometric changes, $f_A \times f_l = \left(\frac{A}{A_0}\right) \times \left\langle \frac{l_0}{l} \right\rangle$, that favor flux and far outpace the rapid loss of driving force $\frac{\Pi + P_t}{\Pi_0}$ that accompanies this chamber size.

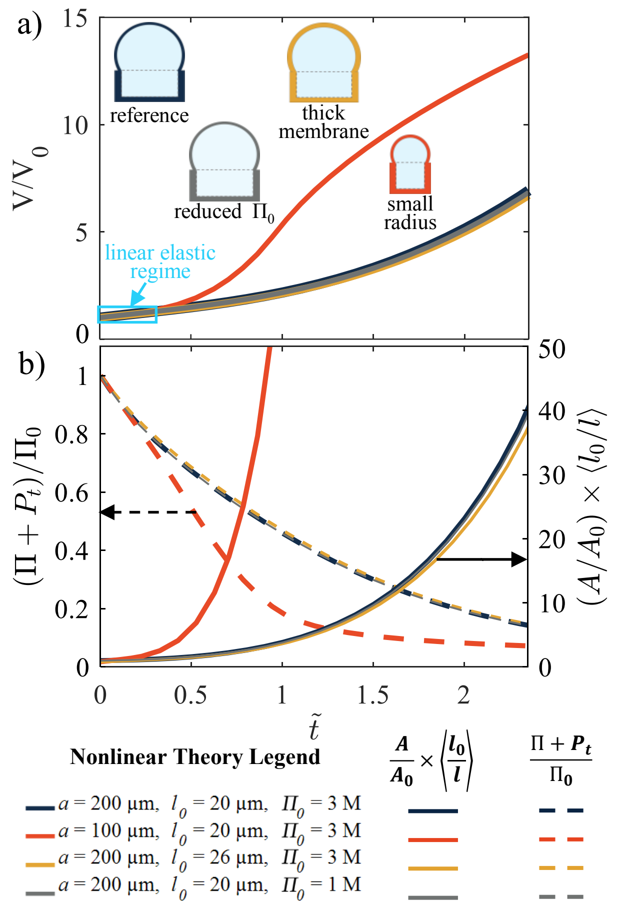

Fig. 4 Predicted time-evolution of chamber volume incorporating large deformation and flux governed by membrane geometry evolution. (a) In dimensionless time $\tilde{t}$ the evolution of chamber volume $\frac{V}{V_0}$ collapses for all experimental configurations except the small radius chamber: reference chamber (navy blue), thick membrane chamber (gold), reduced osmotic loading chamber (gray), and small radius chamber (orange). (Assumptions: Solaris PDMS constitutive response membrane and constant permeability P_w.) (b) The small radius chamber exhibits faster relative actuation due to membrane geometry evolution $f_A f_l = A/A_0 \langle l_0/l \rangle$ (solid) whose nearly 10^3 increase facilitating flow outpaces the faster, but order 1 loss in flow driving force $(\Pi + P_t)/\Pi_0$ inducing flow.

3.6 The permeability of water through PDMS

Using known experimental conditions and independent, fit-mediated membrane mechanics, the only remaining unknown is the permeability P_w. (Mobility L and P_w are related via molecular constants by Eqn. (2).) In this section, we determine P_w in the linear regime for short times, then illustrate improvement upon incorporating nonlinear mechanical behavior for longer times. However, we find that a constant value for the permeability P_w cannot describe the actuators' time-dependent responses.

In all cases, we fit the solution to Eqn. (10) to experimental data normalized by the time-constant τ (Eqn. (9)) using nonlinear least squares fitting. All following results arise from simultaneous fitting of all geometries and osmotic loading. Differing conditions were also fit separately with no significant variation in P_w.

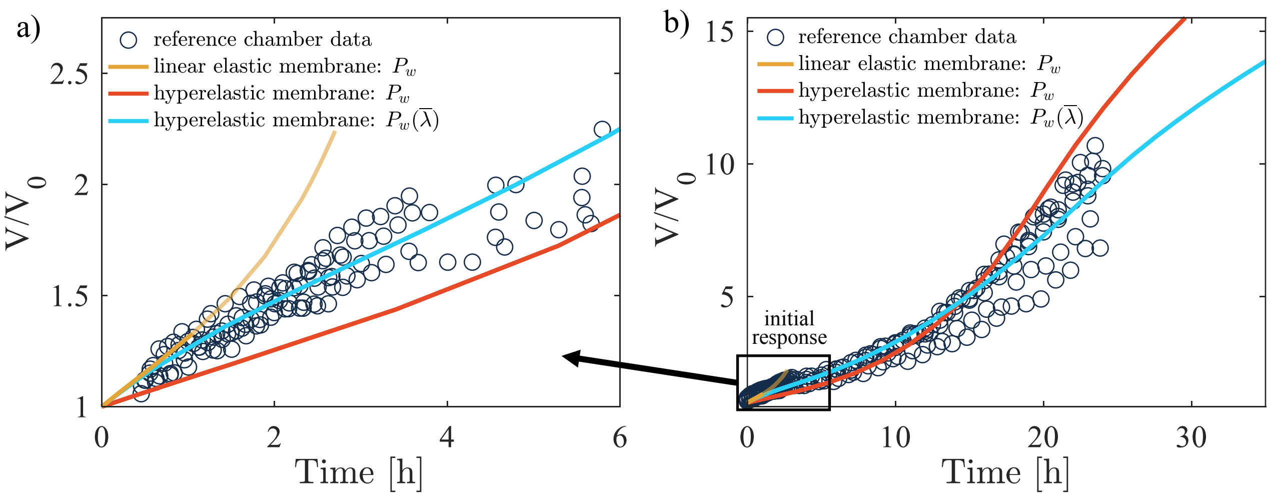

Fig. 5 Fit of experimental data to model. (a) Short- and (b) long-time responses for reference chamber conditions ($a = 200$ μm, $l_0 = 20$ μm, $C_0 = 3$ M) fit to three membrane mechanics/permeability behaviors: linear elastic membrane with constant P_w (gold), hyperelastic membrane with constant P_w (orange), hyperelastic membrane exhibiting stretch-dependent permeability $P_w(\bar{\lambda})$ (teal). The linear elastic response captures the short-time response (dark gold), but overestimates at longer times (light gold extrapolated region). The hyperelastic membrane with constant P_w better captures a moderate stretch response, but underestimates and overestimates at low (a) and high (b) stretches, respectively. A hyperelastic membrane exhibiting stretch-dependent permeability $P_w(\bar{\lambda})$ captures the response (teal) in both regimes (a-b).

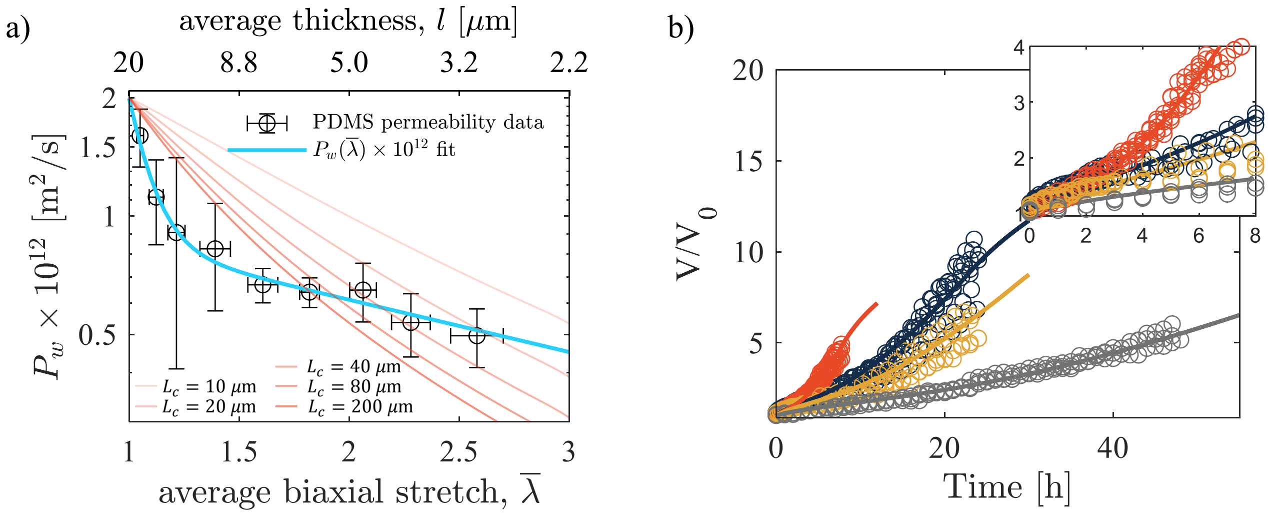

Fig. 6 Deformation-mediated permeability P_w of PDMS. (a) Instantaneous permeability, averaged from all four PDMS chamber conditions, as a function of average biaxial membrane stretch $\bar{\lambda}$ (lower x-axis) and fit to Eqn. (27), teal. Each point (black) represents the average of five instantaneous values, vertical error bars are the standard deviation of the instantaneous permeability values and horizontal error bars are the standard deviation of the average biaxial stretch of each region, where instantaneous permeability values are extracted from segments of 19 experimental $V/V_0(t)$ vs. t curves. This permeability-fit is compared to thickness-dependent (l, upper x-axis) permeability theory expressed by Eqn. (26). Curves for a range of L_c (10-200 μm with increasing orange saturation) capture a significant portion of the deformation-dependent P_w. Each L_c of 10, 20, 40, 80, and 200 μm corresponds to a prediction for $P_{\text{Henry}} \times 10^{12} = 3$, 4, 6, 10, and 22 mm^2/s. (b) Using deformation-dependent permeability, the model (solid lines) captures the time-dependent actuation of all chambers conditions (circles) at both long and short (inset) times.

Table 2 Permeability values from fit

Constitutive Theory & Fit Employed	Permeability, P_w [m^2/s]
Linear Elastic PDMS	$2.02 \cdot 10^{-12}$
Hyperelastic PDMS, constant P_w	$8.35 \cdot 10^{-13}$
Hyperelastic PDMS, $P_w(\bar{\lambda})$	$1.99 \cdot 10^{-12}$ ($\bar{\lambda} = 1$)
Hyperelastic PEO-PDMS, $P_w(\bar{\lambda})$	$1.99 \cdot 10^{-12}$ ($\bar{\lambda} = 1$)

3.6.1 Linear response permeability

Despite the differences in the experimental responses (Fig. 2), at short times (small deformations) the data collapse in dimensionless time as anticipated (ESI†). Using a slightly extended limit ($\tilde{V} < 0.165$; $V/V_0 < 1.3$ for the reference geometry), which corresponds to an approximate biaxial stretch of 1.4 we obtain the gold line in Fig. 5. (The less saturated color extrapolates the linear prediction.) The permeability value for this regime,

2.02×10^{-12} m^2/s, falls at the upper end of values reported in the literature $6 \times 10^{-13} - 2 \times 10^{-12}$ m^2/s[61–63] (Table 2).

3.6.2 Hyperelastic response - constant permeability

Incorporating the hyperelastic mechanical model captures the middle time (moderate deformation) response, but fails to align with the data at short times and overestimates the highly-stretched response region (20-24 h). Figure 5b (dark orange line) illustrates this result, generally capturing the time-dependent data between 10 and 20 h. However at short times (Fig. 5a, dark orange line), the fit falls well below the experimental observations. As a result, the predicted P_w is 58% lower than measured in the linear regime, although it still lies within the lower range of previously measured values.

3.7 A case for deformation-dependent permeability

Given the accuracy of the membrane mechanical response and known osmotic potential for an experimentally-observed bulge, we conclude that capturing the full, time-dependent response requires a stretch-dependent permeability. We motivate the functional form for the deformation-dependence by piecewise instantaneous permeabilities obtained from multiple actuators/geometries. Instantaneous permeability arises by modifying Eqn. (8) with a deformation-dependent mobility term $L(\tilde{V})$, then re-arranging it to obtain

$$L(\tilde{V}) = -\frac{d\frac{V}{V_0}}{dt}\frac{l_0 V_0}{A_0 \Pi_0}\frac{1}{f_A(\tilde{V}) f_l(\tilde{V})}\frac{1}{\left(\frac{1}{\frac{V}{V_0}} + \frac{E f_p(\tilde{V})}{\Pi_0}\right)} \tag{25}$$

which is a function of the instantaneous chamber volume $\tilde{V}$ and the rate of change of deformation $d(V/V_0)/dt$ (ESI† Fig. S9). $L(\tilde{V})$ is converted to permeability using Eqn. (2). Since membrane deformation, rather than bulge volume, is the likely reason for changes in P_w, we re-express $\tilde{V}$ as the *average* biaxial stretch $\overline{\lambda} = \sqrt{A/A_0}$ (ESI†) and the *average* membrane thickness (dropping the thicker $l_0 = 26$ μm geometry). Fig. 6 illustrates the nearly order-of-magnitude decrease in the membrane permeability during the test.

As membranes become thinner, the flux can become dominated by sorption-desorption surface reaction kinetics.[31,33] Firpo, *et al.*[31] expressed the onset of this thickness-dependent behavior using the concept of a critical thickness value L_c in describing gaseous species permeation through PDMS, where $L_c = 2D_w/k_2$[33] and k_2 is the desorption rate constant. Unfortunately, values of k_2 for liquid water from PDMS appear to be lacking in the literature and reported D_w values may or may not be 'apparent' values depending on the membrane thickness used. Thus, we cannot say definitively where our 20 μm films fall with respect to L_c in this system. However, for context, we can employ the functional form for thickness dependent permeability[31]

$$\frac{P}{P_{\text{Henry}}} = \frac{l/L_c}{1 + l/L_c}, \tag{26}$$

where P_{Henry} represents the permeability of the film in the case that Henry's law applies to the surface reactions, *e.g.*, they are *nearly* in equilibrium. We compare this functional form to our thickness-dependent permeability results to assess the likelihood that our observations arise from a similar mechanism (Fig. 6a).

Although permeability monotonically decreases with decreasing thickness, quantitatively and qualitatively Eqn. (26) provides only moderate agreement with our experimentally observed trend (Fig. 6a). Predictive curves are provided for increasing L_c. We constrain Eqn. (26) to pass through the unstretched state ($\overline{\lambda} = 1$, $P_w = 1.99 \times 10^{-12}$ m^2/s). This choice is supported by the robustness of the collapse of the linear response regime (ESI† Fig. S7) and general agreement with previously reported P_w (2×10^{-12} m^2/s, 55 μm thickness[61,63]). This added constraint leads to a predicted P_{Henry} for each L_c. For large L_c, the curve converges to its maximum thickness sensitivity (close to $L_c = 200$ μm) but predicts an order of magnitude higher P_{Henry} than experimentally measured. (Though it has been simulated for mm-thick films, assuming $K_{\text{w:membrane}} \approx 0.1$.[64]) The lower bound for L_c was motivated by CO_2 and He permeants through PDMS; these are on the order of several 10's of μm's. But such small L_c deviate further from experimental observation. We can speculate on the reasons for the discrepancies between Eqn. (26) and our data.

Two potential reasons for a lack of agreement the deformation-dependent-permeability measurements and thickness-dependent permeability predictions are: 1) treating the membrane thickness as an average value and 2) stretch dependent changes in P_w. Though the thickness of a deformed membrane is not uniform, the majority of the film is within 1 μm of the average value (ESI† Fig. S2). Such small variations in film thickness produce relatively minor variations in the thickness-dependent P_w predicted by Eqn. (26). Using $l \pm 1$ μm to create bounds around the smallest and largest L_c predictions, we determine that qualitatively, our above interpretation does not change (ESI† Fig. S10). Therefore, the curves shown in Fig. 6a provide a reasonable representation of thickness-dependent permeability effects, which is likely the greatest, but not only, contributor to the geometry-dependence of P_w. We conclude that effects of stretch may therefore occur as well, though to our knowledge, no theoretical expression for stretch-dependent membrane permeability exists for a solid, rubbery-network, unswollen material. Typically, rubbery membranes are mounted to a rigid substrate[65] or used with moderately swelling solvents.[39] In the former case, little deformation occurs and in the latter, stretch dependence is attributed to changes in conformation of fluid-filled channels. Given the negligible swelling of PDMS in water, the latter are unlikely to be present. Several possibilities include: 1) polymer chains in a stretched configuration may experience a change in mobility that alters 'hopping'[66–68] and 'cluster formation'[36,61,69] mechanisms, 2) deviations from the incompressibility assumption which may mean a slightly higher P_w due to decreased density, but such thicker membranes could be interpreted as a lower P_w than in reality in the current incompressible approach. Future study is required to understand these more subtle effects.

To quantitatively capture the data trend and facilitate comparison within this and later work, we fit our data to the following functional form:

$$P_w(\overline{\lambda}) = C_1 \cdot e^{C_2 \cdot \lambda} + C_3 \cdot e^{C_4 \cdot \lambda} \tag{27}$$

Using this stretch dependence in the time-response ODE captures the experimental volumetric actuation behavior across all timescales for all four experimental geometries as shown in Fig. 6b. The initial permeability at $\overline{\lambda} = 1$ for PDMS is 1.99×10^{-12} [m^2/s], within the range of previously published values and recovering the linear elastic limit. The fit constants are provided in Table 3.

3.7.1 Effects of adding hydrophilic groups

With this means of quantifying mechano-permselectivity accurately, we can evaluate the performance of new material formulations. Previous work suggests that increased permeability is possible through the incorporation of hydrophilic groups within the network solid. One group studied the increased sorption of water into PDMS by adding polyethylene glycol (PEG), finding that PEG could increase the uptake of water from 0.1 to 1.4 wt%.[41] Similarly increased hydrophilicity has been reported in PEO-PDMS composites.[54,70] As a proof-of-concept, we test membranes having 0.5 wt% polyethylene oxide (PEO).

Determination of $P_w(\overline{\lambda})$ in the PEO-PDMS follows the same process outlined in Sec. 3.7. PEO-PDMS membranes are tested using the reference geometry ($a =$ 200 μm, $l_0 =$ 20 μm, $C_0 =$ 3 M); Gent model parameters are in the ESI†; $P_w(\overline{\lambda})$ fit (Fig. 7a, dark blue line) parameters are in Table 3. Figure 7 compares the materials.

We find a moderate increase in P_w (Fig. 7a) and stretch at break in the bulge geometry. Interestingly, this improvement was accompanied by degraded uniaxial tensile mechanical properties, namely a 35% decrease in stretch at break (ESI†, uniaxial and bulge geometries, Fig. S4, S5) which was gathered under dry conditions that may provide one explanation for its poor response. The improved P_w means that PEO-PDMS exhibits a faster actuation rate than PDMS, in spite of its slightly stiffer modulus (+51%) which would provide increased turgor pressure resisting flow. The analysis developed here indicates that the permeability of *undeformed* PMDS and PEO-PDMS vary by only 0.02%, producing similar short time responses. At higher membrane stretch values ($\overline{\lambda} = 3$, $V/V_0 = 7.5$), PEO-PDMS membranes exhibit a 56% larger P_w. It may be that the hydrophilic additions produce only a small increase in the equilibrium sorption behavior (evidenced by similar P_w at $\overline{\lambda} = 1$), but decrease L_c (*e.g.*, via larger k_2).

4 Conclusions

We provide a bulge-based method of determining the stretch-dependent permeation behavior of water through elastomeric membranes. At low deformations, these PDMS membranes exhibit permeability values similar to previously published values.[61,62] However, we find a near order of magnitude decrease at large deformations corresponding to stretch-induced membrane thinning and possibly the stretch itself. Capture of the near order-of-magnitude reduction in both membrane thickness and permeability by a non-equilibrium surface reaction model,[31] implies that geometry-changes provide the primary mechanism for permeability decreases as the bulge grows. The deformation-dependent permeability is replicated for a silicon composite material incorporating hydrophilic PEO groups to the network to provide slightly improved mechano-permselectivity properties.

These results rely upon the fidelity of the mechanical model for the highly bulging membrane and nonlinear, hyperelastic constitutive response. Optical profile matching (Fig. 1) and cross-validation of membrane volume and area time-dependent responses (Fig. 2d) provide evidence of the accuracy of both.

More generally, the approach applies to any thin hyperelastic membrane that can be adhered to a substrate of wells immersed in salt solution. New mechano-permselective functional materials may now be quantitatively evaluated. The microstructural features that optimize these two properties remain an area for future research.

Author Contributions

A. Spitzer performed the investigation, data curation, formal analysis, validation, visualization, and writing (Original Draft Preparation and Review & Editing) of the project. S. Hutchens performed the conceptualization, methodology, funding acquisition, formal analysis, supervision, of the project and contributed to the writing (Review & Editing).

Conflicts of interest

There are no conflicts to declare.

Acknowledgements

This material is based upon work supported by the National Science Foundation under Grant No. (1653676). The material presented in this work was carried out in part in the Micro-Nano-Mechanical Systems Cleanroom Laboratory within the Department of Mechanical Science and Engineering at the University of Illinois.

Notes and references

1 J. A. G. Pais and L. M. G. Ferreira, *Desalination*, 2007, **208**, 269–276.

2 A. Zhu, P. D. Christofides and Y. Cohen, *Journal of Membrane Science*, 2009, **344**, 1–5.

3 G. M. Geise, H. B. Park, A. C. Sagle, B. D. Freeman and J. E. McGrath, *Journal of Membrane Science*, 2011, **369**, 130–138.

4 K. Kimura, N. Ogawa and Y. Watanabe, *Water Science and Technology*, 2013, **67**, 1994–1999.

5 M. Becker, G. Kerstiens and J. Schonherr, *Trees*, 1986, **1**, 54–60.

6 E. Steudle, T. Henzler and U. Bayreuth, *Journal of Experimental Botany*, 1995, **46**, 1067–1076.

7 S. Ong, H. Liu and C. Pidgeon, *Journal of Chromatography A*, 1996, **728**, 113–128.

8 C. Maurel, *Annu. Rev. Plant Physiol. Plant Mol. Biol.*, 1997, **48**, 399–429.

9 Y. Tsujimoto, T. Nakagawa and S. Shimizu, *Biochimica et Biophysica Acta - Bioenergetics*, 2006, **1757**, 1297–1300.

10 J. C. Ellory, H. C. Robinson, J. A. Browning, G. W. Stewart,

Table 3 Stretch Dependent Mobility Function Coefficients

Material	C_1 [m^2/s]	C_2	C_3 [m^2/s]	C_4
Solaris	$2.07 \cdot 10^{-8}$	-9.79	$1.13 \cdot 10^{-12}$	-0.31
PEO-Solaris	$4.85 \cdot 10^{-10}$	-6.27	$1.33 \cdot 10^{-12}$	-0.21

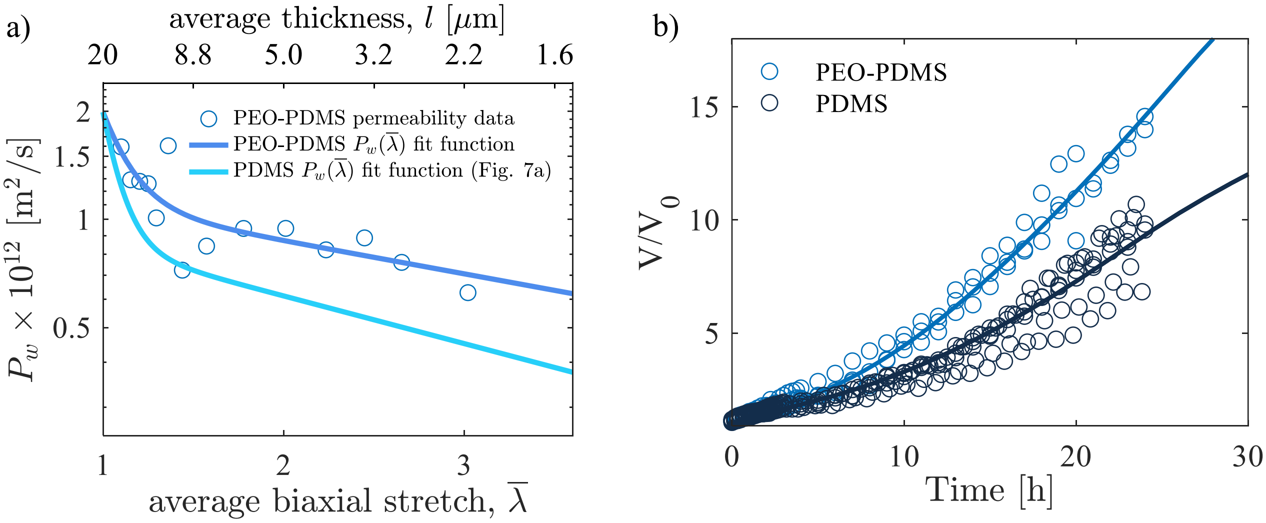

Fig. 7 Comparison of PEO-PDMS and PDMS stretch-dependent permeability $P_w(\overline{\lambda})$. (a) P_w of PEO-PDMS membranes (data: blue circles; fit: dark blue line; chamber conditions: $a = 200\ \mu$m, $l_0 = 20\ \mu$m, $C_0 = 3$ M) exhibit a higher overall permeability than in PDMS (teal line from Fig. 6). Data are the result of three actuating chambers. (b) Accurate modeling of membrane mechanical and permeability properties demonstrate unequivocably that the faster actuation rate of the PEO-PDMS chamber (light blue) arises from permeability and not simply from a difference in constitutive behavior. Both membranes use the reference chamber configuration.

K. A. Gehl and J. S. Gibson, *Blood Cells, Molecules, and Diseases*, 2007, **39**, 1–6.
11 W. Shinoda, *Biochimica et Biophysica Acta - Biomembranes*, 2016, **1858**, 2254–2265.
12 Y. C. Su and L. Lin, *Journal of Microelectromechanical Systems*, 2004, **13**, 75–82.
13 E. Sinibaldi, G. L. Puleo, F. Mattioli, V. Mattoli, F. Di Michele, L. Beccai, F. Tramacere, S. Mancuso and B. Mazzolai, *Bioinspiration and Biomimetics*, 2013, **8**, 025002.
14 E. Sinibaldi, A. Argiolas, G. L. Puleo and B. Mazzolai, *PLoS ONE*, 2014, **9**, 102461.
15 H. Yuk, S. Lin, C. Ma, M. Takaffoli, N. X. Fang and X. Zhao, *Nature Communications*, 2017, **8**, year.
16 H. Hsu, L. Y. Liu, L. Y. Liu and Y. C. Su, *Smart Materials and Structures*, 2018, **27**, 084006.
17 I. Must, E. Sinibaldi and B. Mazzolai, *Nature Communications*, 2019, **10**, 1–8.
18 A. Kataruka and S. B. Hutchens, *Matter*, 2021, **4**, 3991–4005.
19 H. Na, Y. W. Kang, C. S. Park, S. Jung, H. Y. Kim and J. Y. Sun, *Science*, 2022, **376**, 301–307.
20 M. Schanz, *Applied Mechanics Reviews*, 2009, **62**, year.
21 M. L. Oyen, *International Materials Reviews*, 2014, **59**, 44–59.
22 D. Caccavo, S. Cascone, G. Lamberti and A. A. Barba, *Chem. Soc. Rev.*, 2018, **47**, 2357.
23 A. M. Reeve, M. P. Nash, A. J. Taberner and P. M. F. Nielsen, *Journal of Biomechanical Engineering*, 2014, **136**, 1–9.
24 D. Sachs, A. Wahlsten, S. Kozerke, G. Restivo and E. Mazza, *Biomechanics and Modeling in Mechanobiology*, 2021, **20**, 969–982.
25 Y. Leng, M. D. Lucio and H. Gomez, *Computer Methods in Applied Mechanics and Engineering*, 2021, **384**, 113919.
26 J. Wijmans and R. Baker, *Journal of Membrane Science*, 1995, **107**, 1–21.
27 Y. J. Lin, P. Dias, H. Y. Chen, A. Hiltner and E. Baer, *Polymer*, 2008, **49**, 2578–2586.
28 I. Özen, G. Bozoklu, C. Dalgıçdir, O. Yücel, E. Ünsal, M. Çakmak and Y. Z. Menceloğlu, *European Polymer Journal*, 2010, **46**, 226–237.
29 S. Sato, M. Suzuki, S. Kanehashi and K. Nagai, *Journal of Membrane Science*, 2010, **360**, 352–362.
30 P. Peng, B. Shi, Y. Lan, P. Peng, B. Shi and Y. Lan, *Separation Science and Technology*, 2011, **6395**, 234–246.
31 G. Firpo, E. Angeli, L. Repetto and U. Valbusa, *Journal of Membrane Science*, 2015, **481**, 1–8.
32 P. Bian, Y. Wang and T. J. McCarthy, *Macromolecular Rapid Communications*, 2021, **42**, 1–5.
33 M. A. Islam, H. Buschatz and D. Paul, *Journal of Membrane Science*, 2002, **204**, 379–384.
34 M. Muller and V. Abetz, *Chemical Reviews*, 2021, **121**, 14189–14231.
35 B. J. Zwolinski, H. Eyring and C. E. Reese, *Journal of Physical and Colloid Chemistry*, 1949, **53**, 1426–1453.
36 Y. Tamai, *Macromolecules*, 1994, **27**, 4498–4508.
37 C. S. Vidmar, M. Bazzi and V. K. Lai, *Journal of the Mechanical*

Behavior of Biomedical Materials, 2022, **128**, 105107.

38 M. S. Chun and D. Y. Lee, *Bulletin of the Korean Chemical Society*, 2015, **36**, 269–275.

39 R. Song, H. A. Stone, K. H. Jensen and J. Lee, *Journal of Fluid Mechanics*, 2019, 742–754.

40 S. Lee, H.-y. Lee, I.-f. Lee and C.-y. Tseng, *European Journal of Physics*, 2004, **25**, 331–336.

41 A. I. Panou, K. G. Papadokostaki, P. A. Tarantili and M. Sanopoulou, *European Polymer Journal*, 2013, **49**, 1803–1810.

42 M. P. Milner, L. Jin and S. B. Hutchens, *Soft Matter*, 2017, **13**, 6894–6904.

43 A. Souza, E. Marques, C. Balsa and Joao Ribeiro, *applied sciences*, 2020, **10**, 3322.

44 B. Zhang and S. B. Hutchens, *Soft Matter*, 2021, **17**, 6728–6741.

45 E. Yang, M. Zhang, J. Zeng and F. Tian, *Soft Matter*, 2022, **18**, 5465–5473.

46 K. Song, N.-K. Cho, K. Park and C.-S. Kim, *Polymers*, 2022, **14**, 2373.

47 M. Darestani, J. Locq and G. J. Millar, *Separation Science and Technology (Philadelphia)*, 2019, **54**, 128–142.

48 D. C. Pamplona and D. E. Mota, *International Journal of Mechanical Sciences*, 2012, **65**, 18–23.

49 T. Gopesh and J. Friend, *Soft Robotics*, 2021, **8**, 365–370.

50 A. Das, K. S. Breuer and V. Mathai, *Applied Physics Letters*, 2020, **116**, year.

51 M. Sasso, G. Palmieri, G. Chiappini and D. Amodio, *Polymer Testing*, 2008, **27**, 995–1004.

52 A. P. Selvadurai and M. Shi, *International Journal of Non-Linear Mechanics*, 2012, **47**, 228–239.

53 R. Long, K. R. Shull and C. Y. Hui, *Journal of the Mechanics and Physics of Solids*, 2010, **58**, 1225–1242.

54 D. B. Thompson, A. S. Fawcett and M. A. Brook, Silicon Based Polymers: Advances in Synthesis and Supramolecular Organization, 2008, pp. 29–38.

55 Y. Xia and G. M. Whitesides, *Annu. Rev. Mater. Sci*, 1998, **28**, 153–84.

56 J. A. Barrie and D. Machin, *Journal of Macromolecular Science, Part B*, 1969, **3**, 645–672.

57 S. Timoshenko and S. Woinowsky-Krieger, *Theory of plates and shells*, McGraw-Hill, 1959, p. 580.

58 J. J. Vlassak and W. D. Nix, *J. Mater. Res*, 1992, **7**, 3242–3249.

59 A. Libai and J. Simmonds, *The Nonlinear Theory of Elastic Shells*, Cambridge University Press, New York, 1998.

60 A. N. Gent, *International Journal of Non-Linear Mechanics*, 2005, **40**, 165–175.

61 J. M. Watson and M. G. Baron, *Journal of Membrane Science*, 1996, **110**, 47–57.

62 G. C. Randall and P. S. Doyle, *PNAS*, 2005, **102**, 10813–10818.

63 S. J. Harley, E. A. Glascoe and R. S. Maxwell, *Journal of Physical Chemistry B*, 2012, **116**, 14183–14190.

64 C. Lu, Y. Sun, S. Harley and E. Glascoe, *TOUGH Symposium 2012*, 2012, 8.

65 H. Held and S. Landi, *Journal of Biological Standardization*, 1977, **5**, 111–119.

66 R. M. Sok, H. J. Berendsen and W. F. Van Gunsteren, *The Journal of Chemical Physics*, 1992, **96**, 4699–4704.

67 J. J. Lange, C. T. Culbertson and D. A. Higgins, *Analytical Chemistry*, 2008, **80**, 9726–9734.

68 A. E. Ismail, G. S. Grest, D. R. Heine and M. J. Stevens, *Marcomolecules*, 2009, **42**, 3186–3194.

69 J. A. Barrie and B. Platt, *Polymer*, 1963, **4**, 303–313.

70 B. K. D. Ngo, K. K. Lim, S. J. Stafslien and M. A. Grunlan, *Polymer Degradation and Stability*, 2019, **163**, 136–142.

Soft Matter

ARTICLE TYPE

Cite this: DOI: 00.0000/xxxxxxxxxx

Electronic Supplementary Information: Deformation-dependent polydimethylsiloxane permeability measured using osmotic microactuators

Alexandra R. Spitzer[a] and Shelby B. Hutchens[a,b,*]

Received Date
Accepted Date

DOI: 00.0000/xxxxxxxxxx

1 Chemical Potential Driven Flux through a Membrane

1.1 Chemical Potential

Chemical potential, μ, is defined as,

$$\mu = \mu_o + RT\,ln(\chi_l \gamma_l) \tag{1}$$

where μ_o is the reference chemical potential, χ_l is the mole fraction of the solvent, and γ_l is the activity coefficient of the solvent, R is the universal gas constant, and T is the temperature.

1.2 Diffusive Flux Through a Membrane

Flux of the diffusive species water, J_w, is defined as,

$$J_w = -L_w \frac{d\mu_w}{dx} \tag{2}$$

where, L_w is the mobility of the diffusive species water, and $\frac{d\mu_w}{dx}$ is the driving force of water, described by the change in the chemical potential of water across the thickness dimesnion of the membrane, x.

$$J_w \propto \frac{-d\mu_w}{dx} \propto -\frac{\mu_2 - \mu_1}{l} \tag{3}$$

The flux of water across a membrane, is therefore proportional to the chemical potential difference across that membrane. This can be described by the difference of the chemical potentials of solution separated by the membrane, μ_1 and μ_2, which has a thickness of l.

This difference in chemical potential on either side of the membrane and resulting non-equilibrium condition, serves as the driving force for the flux of water across the membrane toward chemical equilibrium between solutions separated by the membrane. To understand the difference in chemical potential between the encapsulated salt solution and pure water reservoir, the chemical potentials of each of the individual solutions must be defined. For low solute concentrations, the activity coefficient of water, γ_{w}, is approximately 1. Here $\chi_{w,pure}$ describes the mole fraction of pure water, and $\chi_{\mathrm{w,salt\ solution}}$ describes the mole fraction of the water in the salt solution.

$$\mu_{\mathrm{w,pure}} = \mu_{\mathrm{o,water}} + RT\ln\left(\chi_{\mathrm{w,pure}}\right) \tag{4}$$

$$\mu_{\mathrm{w,salt\ solution}} = \mu_{\mathrm{o,water}} + RT\ln\left(\chi_{\mathrm{w,salt\ solution}}\right) \tag{5}$$

Subtracting equation 5 from 4, will result in the chemical potential difference between the pure water and salt solution.

$$\mu_{\mathrm{w,pure}} - \mu_{\mathrm{w,salt\ solution}} = RT\ln\left(\chi_{\mathrm{w,pure}}\right) - RT\ln\left(\chi_{\mathrm{w,salt\ solution}}\right) \tag{6}$$

The mole fraction of solvent in pure water is $\chi_{\mathrm{w,pure}} = 1$, so that $RT\ln(1) = 0$. The chemical potential of pure water, $\mu_{\mathrm{w,pure}}$, can alternatively be referred to as the reference chemical potential for water, μ_o, and therefore we denote $\mu_{\mathrm{w,salt\ solution}}$, as μ. Combining these statements with equation 6 results in:

$$\mu{=}\mu_o + RT\ln\left(\chi_{\mathrm{w,salt\ solution}}\right) \tag{7}$$

For a solution with a low solute mole fraction, χ_{salt}, the mole fraction of solvent, $\chi_{\mathrm{w,salt\ solution}}$, is relatively high. This solvent mole fraction can alternatively be expressed as $1 - \chi_{\mathrm{salt}}$.

$$\mu = \mu_o + RT\ln\left(1 - \chi_{\mathrm{salt}}\right) \tag{8}$$

For small values of χ_{salt}, a Taylor series expansion can be used, yielding

$$\mu = \mu_o + RT\ln\left(-\chi_{\mathrm{salt}}\right) \tag{9}$$

This salt mole fraction can be expressed as the ratio of moles of salt present, n_{salt}, to the total moles present in solution, $n_{\mathrm{salt}} +$

---

[a] *Department of Materials Science and Engineering, University of Illinois Urbana-Champaign, Urbana, IL, USA.*

[b] *Department of Mechanical Science and Engineering, University of Illinois Urbana-Champaign, Urbana, IL, USA. E-mail: hutchs@illinois.edu; Tel: +1 (217)300-0412*

n_{water}.

$$\mu = \mu_o + RT\ln\left(-\frac{n_{\text{salt}}}{n_{\text{salt}}+n_{\text{water}}}\right) \tag{10}$$

The osmotic potential of a solution, as defined by Van't Hoff, describes the pressure necessary to keep solvent from flowing into a a concentrated region,

$$\Pi = -i\frac{n_{\text{salt}}}{V}RT, \tag{11}$$

where i is the electronic dissociation factor of the ionic solute.

Combing equations 10 and 11, results in the following expression relating the chemical potential to the osmotic potential and and solution properties, where $V_m = \frac{V}{n_{\text{water}}}$ and describes the molar volume of water .

$$\mu = \mu_o + \frac{\Pi V}{n_{water}} = \mu_0 + \Pi V_m \tag{12}$$

The reference chemical potential depends on the systems' pressure, $P = P_{atm} + P_t$. Here P_{atm} describes the atmospheric pressure, and P_t describes the turgor pressure or hydrostatic pressure on one or both sides of a membrane. Understanding this dependence, Equation 12, can be written to explicitly indicate pressure terms,

$$\mu = \mu_0(P_{atm}+P_t) + \Pi V_m. \tag{13}$$

At a constant temperature, Gibb's free energy is defined as, $d\mu = VdP - SdT$. We assume constant temperature and constant atmospheric pressure, allowing for the re-expression of 13 as,

$$\mu = \mu_0(P_{atm}) + \Pi V_m + \int_{P_{atm}}^{P_{atm}+P_t} V_m(P)dP \tag{14}$$

For an incompressible substance, which is a reasonable approximation for water over the range of pressures we attain, this integral reduces to V_mP_t, resulting in,

$$\mu = \mu_0(P_{atm}) + \Pi V_m + V_mP_t \tag{15}$$

This can rearranged to form the expression,

$$\mu - \mu_0 = V_m(P_t + \Pi) \tag{16}$$

Combining Equations 2 and 16, results in a pressure dependent equation for diffusive flux of species i through a membrane, which is expressed in units of $\frac{mol}{m^2s}$.

$$J_w = \frac{-L_wV_m}{l}(\Pi + P_t) \tag{17}$$

1.3 Diffusive Flux and Diffusivity Relationship

When discussing permeability and diffusion of a species, such as water within a membrane, a common term referred to is diffusivity, D_w, which describes the rate at which a species can diffuse through the area of a membrane $[\frac{m^2}{s}]$. Diffusivity is the term that relates the diffusive flux, J_w, to the concentration gradient, $\frac{du_w}{dx}$ that serves as the driving force, as opposed the the chemical potential difference as in the previous section.

$$J_w = -D_w\frac{dC_w}{dx} \tag{18}$$

Diffusivity, D_w, can be related to the mobility, L_w of water within the membrane. From the definition of chemical potential, diffusive flux can be redefined in terms of mole fraction of water, $\chi_w = C_wV$, where C_w is the concentration of water, in volume V.

$$J_w = -L_wRT\frac{dln\chi_w}{dx} = -L_wRT\frac{dln(C_wV)}{dx} = -\frac{L_wRT}{C_w}\frac{dC_w}{dx} \tag{19}$$

This results in the following relationship for mobility in terms of diffusivity,

$$L_w = \frac{D_wC_w}{RT} \tag{20}$$

1.4 Permeability and Diffusivity

In the determination of the rate of flux of a species through a memembrane, two terms are commonly used: diffusivity and permeability. However, these terms are not interchangeable. The diffusivity describes the flux of the water while it is within the membrane, but the permeability encompasses the full membrane, including transport of molecules from the surrounding reservoir into the membrane and transport out of the membrane to the other reservoir. For this reason, in membrane literature, the diffusive flux of water is often described using permeability coefficient prefactor, as follows,

$$J_w = -P_w\frac{dC_w}{dx} \tag{21}$$

In this case, P_w, the permeability coefficient is equal to,

$$P_w = D_wK_{\text{w:membrane}} \tag{22}$$

where D_w is the diffusivity that was described in the previous section, and $K_{w:membrane}$ is known as the sorption or partition coefficient of water and the membrane. Here, the sorption describes the ratio of concentrations of two separate components in in the membrane (the membrane matrix, and the diffusive species). In our case, water must dissolve into the membrane from the feed solution, diffuse through the membrane's thickness and then dissolve out of the membrane into the chamber solution. This solubility quantity describes how much water can dissolve into the membrane and will in turn affect the rate of permeation. As we are unable to measure the the content of water in our films, so we can only fit the permeability coefficient. Therefore, we redefine our mobility relationship, using the permeability coefficient, instead of diffusivity, as the rate of diffusion of water through our membrane which also depends on the sorption of water into PDMS.

$$L_w = \frac{P_wC_w}{RT} \tag{23}$$

1.5 Volumetric Flux Through a Membrane

To relate the volume of a species diffusing across a membrane of a given area, we must relate the diffusive flux, J_w, expressed in units $[\frac{\text{mol}}{m^2\cdot s}]$, to a volumetric flux, which we will refer to as J_Q, expressed in units of $[\frac{m^3}{m^2\cdot s}]$. This can be done by relating the diffusive flux, to the molecular weight of the the solution, M_w, and the density of the solution ρ.

$$J_Q = \frac{J_w M_W}{\rho} \tag{24}$$

Using this new volumetric flux relationship, we define a volumetric diffusivity for water through our membrane, using the relationships we have described thus far. We combine Equations 17, 20, and24, resulting in,

$$J_Q = -\frac{P_w C_w}{RT}\frac{V_m M_W}{\rho}\frac{(\Pi + P_t)}{l} = -L_w \frac{V_m M_W}{\rho}\frac{(\Pi + P_t)}{l} \tag{25}$$

We define a volumetric mobility, which we denote as L, describing the mobility rate of a volume of water to diffuse through the an area of the membrane per the pressure applied to the membrane. This term is directly related to the permeability coefficient. L is expressed in units $[\frac{m^2}{Pa \cdot s}]$.

$$L = \frac{P_w C_w}{RT}\frac{V_m M_W}{\rho} = L_w \frac{V_m M_W}{\rho} \tag{26}$$

Our new equation expression describing volumetric flux through the membrane, is defined as,

$$J_Q = -\frac{L}{l}(\Pi + P_t) \tag{27}$$

Thus J_Q is expressed in units $[\frac{m^3}{m^2 \cdot s}]$ or $[\frac{m}{s}]$.

2 Ion Diffusion Time Scale for Well-mixed Chamber

We determine that the actuation chambers that we study are well mixed by calculating the time scale for a single sodium ion to diffuse from one side of the chamber to the other. The height of all the chambers is constant with dimensions of $h = 110\ \mu$m. We use this chamber height as the diffusion length scale, determining the time for a single osmolyte ion to travel the from the membrane to chamber floor. This is calculated assuming Fickian diffusion and the Einstein-Smoluchowski Equation:

$$D = \frac{l^2}{2t} \tag{28}$$

where D is the diffusivity of the species, in this case a sodium ion, l is the diffusion length which in this system in the height of the chamber ($h = 110\ \mu$m), and t is the time it takes for this species to diffuse across this length scale. For sodium ions Na^+ the diffusivity in water is $D = 2.098 \times 10^{-9}$ [units:$\frac{m^2}{s}$].[1] Using this information, we solve for $t = 2.88$ s. This short time scale for diffusion across the initial depth of the chamber, leads to our assumption that osmolyte ions in our system can diffuse away from the membrane quickly, meaning that the chamber is well-mixed.

3 Osmotic Pressure Term

The change in osmotic pressure due to the water flow into the chamber is described by the difference in osmotic potential between the chamber and the surrounding feed solution, at a given time.

$$\Delta\Pi(t) = -iRT\left(\frac{n_s}{V(t)} - C_{\text{feed}}\right) \tag{29}$$

The explicit time dependence of this expression can be removed by non-dimensionalizing the volume term by the initial chamber volume V_0, which is the only time dependent term. This nondimensionalized term is the volume ratio of the chamber described by $V(t) = V_0 \frac{V}{V_0}$. At any given instant, the entire volume of the chamber (both the volume under the membrane in addition to the undeformed chamber volume) is described by the non-dimensionalized volume multiplied by the initial chamber volume. The osmotic pressure term can therefore be described by the following expression, removing the time-dependent terms.

$$\Delta\Pi = -iRT\left(\frac{n_s}{(V/V_0)V_0} - C_{\text{feed}}\right) \tag{30}$$

The initial concentration of salt solution encapsulated into the chamber, C_0, is defined as the initial molar quantity of salt in the chamber, n_s, divided by the initial volume of the chamber, V_0. The term $\frac{n_s}{V_0}$ can be replaced by C_0, and factored out of both osmotic pressure terms.

$$\Delta\Pi = -iRTC_0\left(\frac{1}{V/V_0} - \frac{C_{\text{feed}}}{C_0}\right) \tag{31}$$

Finally, as previously discussed the osmotic potential defined by Van't Hoff is $\Pi = -iRTC$, meaning $-iRTC_0$ can be replaced by the initial chamber osmotic potential Π_0. This initial osmotic pressure term can be factored out of the entire expression, to leave an dimensionless osmotic pressure term.

$$\frac{\Delta\Pi}{\Pi_0} = \frac{1}{V/V_0} - \frac{C_{\text{feed}}}{C_0} \tag{32}$$

However, in this system, we utilize a pure water feed solution $C_{\text{feed}} = 0$, meaning $\frac{C_{\text{feed}}}{C_0} = 0$. This leaves the final form of the osmotic pressure term as,

$$\frac{\Delta\Pi}{\Pi_0} = \frac{1}{V/V_0}. \tag{33}$$

4 Linear Elastic Membrane Parameters

We develop a set of membrane bulge parameters to describe the deformation and volume evolution of the system, in terms of linear elastic membrane deformation.

4.0.1 Linear Elastic Surface Area Parameter

Water flow through the selectively permeable membrane results in membrane deformation. The volumetric flow of water is dependent on the surface area of the membrane. This surface area is changing as the membrane is bulging, and therefore we determine the changing surface area with linear elastic behavior, to understand the volume flow rate of water through the membrane. This stretching is time-dependent, and just like previously described, we aim to non-dimensionalize in order to remove the explicit time-dependence. To describe the linear elastic bulging and resulting membrane stretching we use spherical cap geometry relationships. The time-dependent change in this linear elastic membrane is described by the following expression,

$$A(t) = \pi a^2 + \frac{4(V(t) - V_0)^2}{a^4}, \tag{34}$$

where a, is the constant radius of the cylindrical chamber, $V(t)$ is the time dependent volume of the chamber, and V_0 is the initial volume of the chamber at $t = 0$.

The surface area term can be non-dimensionalized by eliminating the time dependence of the volume. This deformation, while explicitly time-dependent is also a function of the membrane bulge volume. For this reason we introduce a dimensionless membrane bulge volume parameter $\tilde{V}$ that quantifies the approximate deflection of the membrane, with respect to the membrane's initial volume V_0, initial area A_0, and chamber radius a, as described by:

$$\tilde{V} = \frac{V(t) - V_0}{A_0 a} = \frac{\frac{V}{V_0} - 1}{\frac{A_0 a}{V_0}} = \frac{\frac{V}{V_0} - 1}{\frac{A_0 a}{V_0}} \tag{35}$$

To nondimensionalize with the membrane deflection parameter we must reconfigure the surface area expression to use the same terms. First, we can nondimensionalize the entire expression, by the initial membrane surface area, $A_0 = \pi a^2$, to determine the normalized change in surface and introduce the A_0 term into the expression. In addition to this we can remove the explicit time-dependence using the same volume ratio term as described previously, $V(t) = V_0 \frac{V}{V_0}$. Employing both of these changes results in the following expression:

$$\frac{A}{A_0} = 1 + \frac{4(\frac{V}{V_0} - 1)^2}{\frac{A_0 a^4}{{V_0}^2}}, \tag{36}$$

This expression can now be related to $\tilde{V}$ the dimensionless membrane deflection term, as $\tilde{V}^2$ can be factored out the expression as follows resulting in a dimensionless membrane surface area expression as a function of $\tilde{V}$.

$$\frac{A(\tilde{V})}{A_0} = 1 + \frac{4A_0\tilde{V}^2}{a^2} \tag{37}$$

4.1 Turgor Pressure Parameter

As water flows through the membrane and the membrane deflects, turgor pressure P_t builds to maintain a static equilibrium. To analytically understand this term with the use of linear elastic mechanics, we follow the assumptions of the Timoshenko theory describing the linear-elastic bulging of a spherical cap[2] as a function of volume change while using the Nix approximation[3]. The increasing volume due to the membrane bulging V_{BM} using this method is described by,

$$V_{BM} = \frac{\pi h}{6}(3a^2 + \delta^2) \approx \frac{\pi a^2 \delta}{2}, \tag{38}$$

where a is the radius of the membrane, δ is the vertical deflection of the membrane center. This Nix approximation holds true for small deflections where $\delta \ll a$. This volume can also be described by subtracting initial chamber volume V_0, from total time-dependent volume of the chamber and added volume under the membrane $V(t)$. This can be nondimensionalized to remove explicit time-dependence using the same nondimensionalization scheme we have utilized previously.

$$V_{BM} = V(t) - V_0 = V_0\frac{V}{V_0} - V_0 = V_0\left(\frac{V}{V_0} - 1\right) \tag{39}$$

In addition to this approximation, we use Timoshenko's linear elastic theory to describe the hydrostatic biaxial pressure in the circular bulging membrane. This can also be referred to as the linear elastic turgor pressure, P_t.

$$p - p_{atm} = P_t = \frac{8Yl_0\delta^3}{3a^4}, \tag{40}$$

where Y is the biaxial modulus of the membrane and l_0 is the membrane thickness. The biaxial modulus is related to Young's modulus as $Y = E/(1-\nu)$, and it is assumed that the membrane used is incompressible, meaning $\nu = 0.5$, simplifying the relationship to $Y = 2E$.

The vertical displacement of the bulging membrane at the center δ, can be solved for using Eqns. 38, 39, and expressed as a function of the dimensionless deflection term $\tilde{V}$.

$$\delta = \frac{2V_0(\frac{V}{V_0} - 1)}{\pi a^2} = \frac{2(\frac{V}{V_0} - 1)}{\frac{A_0}{V_0}} = 2\tilde{V}a \tag{41}$$

This new expression for δ is substituted into 40, resulting in the following relationship for turgor pressure as a function of dimensionless stretch term $\tilde{V}$:

$$P_t(\tilde{V}) = \frac{16El_0 2\tilde{V}a^3}{3a^4} = \frac{128}{3}\frac{El_0\tilde{V}^3}{a}. \tag{42}$$

However, this term still has units of pressure [Pa]. We normalize the entire term the Young's modulus E [units:Pa], resulting in fully a nondimensionlized turgor pressure parameter.

$$\frac{P_t(\tilde{V})}{E} = \frac{128}{3}\frac{l_0\tilde{V}^3}{a}. \tag{43}$$

5 Hyperelastic Membrane Parameters

We analytically solve for the bulging membrane deformation profile, by parameterizing the undeformed membrane, and solving 5 ODE governing equations that give the solution for the deformed profile as well as the turgor pressure, P_t that causes the deformation. Here we discuss how we utilize the deflection profile solutions to determine hyperelastic membrane deformation parameters utilized in the volume flow rate ODE.

5.1 Non-dimensionalization of membrane geometry parameters

We nondimensionalize all of our geometric membrane parameters for ease of calculation. However, some of the finalized calculations for the stretched membrane constitutive responses rely on quantities with dimensions (surface area, thickness, etc.). Here we define the dimensionless term and their reliance on quantities with dimension, so going forward the two can be converted between with ease.

We non-dimensionalize all initial geometric quantities by the initial radius of the undeformed membrane a, resulting in the nondimensionalized terms,

$$\tilde{r} = \frac{r}{a}, \qquad \tilde{z} = \frac{z}{a}, \qquad \rho = \frac{\rho'}{a}, \qquad \tilde{\xi} = \frac{\xi}{a}, \tag{44}$$

where the dimensional terms are r (the horizontal coordinate system), z (the vertical coordinate system), ρ' (the initial undeformed parameterized membrane coordinates), and ξ (the membrane arc-length). Therefore, we can further define $\frac{d\rho}{d\rho'} = \frac{1}{a}$, which will aide in further verification of this nondimensionalization method.

With respect to the nondimensionlizing volume, we maintain the same nondimensionalization scheme previously defined for the bulging membrane volume where,

$$\tilde{V} = \frac{V_{\text{deformed bulge}}}{\pi a^3}. \tag{45}$$

To nondimensionalize all the governing equations it is important to check that all stretch ratios with defined with new dimensionless parameters remain dimensionless. First, we verify the longitudinal stretch ratio defined by the change in arc-length ξ over the change in the initial membrane position ρ', can be defined the with the equivalent dimensionless terms ($\tilde{\xi}$,ρ).

$$\lambda_\xi = \frac{d\xi}{d\rho'} = \frac{d(a\tilde{\xi})}{d\rho'} \frac{\frac{1}{a}}{(\frac{d\rho}{d\rho'})} = \frac{d\tilde{\xi}}{d\rho} \tag{46}$$

We verify the latitudinal stretch ratio defined as the r-coordinate over the initial membrane position ρ' is equivalent when defined with $\tilde{r}$ and ρ.

$$\lambda\phi = \frac{r}{\rho'} = \frac{\tilde{r}a}{\rho a} = \frac{\tilde{r}}{\rho} \tag{47}$$

5.2 Determining the Hyperelastic Bulge Volume

The dimensionless deflection $\tilde{V}$ of the deformed profile is calculated from the device volume gained as a result of the bulging membrane volume, which we input as a boundary condition to solve for the deformed profile. The dimensionless volume is described by the 5th governing equation (Eqn. 48) developed, where $\tilde{V}$ can be found via integration along the $\tilde{z}$ axis for ‘disks’ of radius $\tilde{r} = \rho\lambda_\phi$.

$$\frac{d\tilde{V}}{d\rho} = \lambda_\phi \rho^2 \frac{d\tilde{z}}{d\rho} \tag{48}$$

5.3 Determining the Hyperelastic Bulging Membrane Surface Area

We determine the dimensionless surface area of each deformed profile $\frac{A}{A_0}$ by integrating over a differential element of length $d\tilde{\xi}(\rho)$ of the deformed membrane from $0 \le \rho \le 1$, given by the expression,

$$d\tilde{\xi}(\rho) = \lambda_\xi(\rho) d\rho. \tag{49}$$

This line segment is revolved from $0 \le \phi \le 2\pi$ at a radius $\tilde{r} = \lambda_\phi \rho$ about the $\tilde{z}$-axis to obtain an expression for the dimensionless area, $\tilde{A}$. This can be normalized by the initial dimensionless area, $\tilde{A}_0 = \frac{A_0}{a^2}$, yielding,

$$\frac{A}{A_0} = \frac{\tilde{A}}{\tilde{A}_0} = \frac{a^2 \int_0^{2\pi} \int_0^{\tilde{\xi}(1)} d\tilde{\xi}\tilde{r} d\phi}{A_0} = \frac{2\pi a^2 \int_0^1 \lambda_\xi(\rho)\lambda_\phi(\rho)\rho \, d\rho}{A_0}. \tag{50}$$

5.4 Determining the Hyperelastic Bulging Membrane’s Average Thickness

We calculate the dimensionless inverse average membrane thickness $\langle l_0/l \rangle$ across the entire membrane area by multiplying the expectation value

$$\left\langle \frac{1}{l} \right\rangle = \frac{2\pi a^2 \int_0^1 \frac{1}{l(\rho)} \lambda_\xi(\rho)\lambda_\phi(\rho)\rho \, d\rho}{A} \tag{51}$$

by the initial thickness l_0. Where $l(\rho) = l_0\lambda_r(\rho)$ and invoking incompressibility $\lambda_r\lambda_\xi\lambda_\phi = 1$ gives the final expression

$$\left\langle \frac{l_0}{l} \right\rangle = \frac{2\pi a^2 \int_0^1 (\lambda_\xi(\rho)\lambda_\phi(\rho))^2 \rho \, d\rho}{A} \tag{52}$$

For completeness, we compare the average membrane thickness values $\frac{1}{\langle 1/l \rangle}$ and $\langle l \rangle$ and find that in our case, these quantities are nearly interchangeable. First, we define

$$\langle l \rangle = \frac{2\pi a^2 \int_0^1 l_0 \lambda_r \lambda_\xi \lambda_\phi \, d\rho}{A} = \frac{\pi l_0 a^2}{A} = l_0 \frac{A_0}{A}. \tag{53}$$

Fig. S1 plots the inverse of Eqn. 51 and Eqn. 53 as functions of $\tilde{V}$ for the Solaris constitutive parameters and the reference chamber geometry. At greater values of $\tilde{V}$, which corresponds to greater membrane stretching, there is a small deviation between these two approaches to calculating normalized average thicknesses. The normalized average thickness given by $\frac{1}{\langle l_0/l \rangle}$ is predicted to be slightly less than the value predicted by $\frac{1}{l_0/\langle l \rangle}$. We use $\frac{1}{l_0/\langle l \rangle}$ to be more precise.

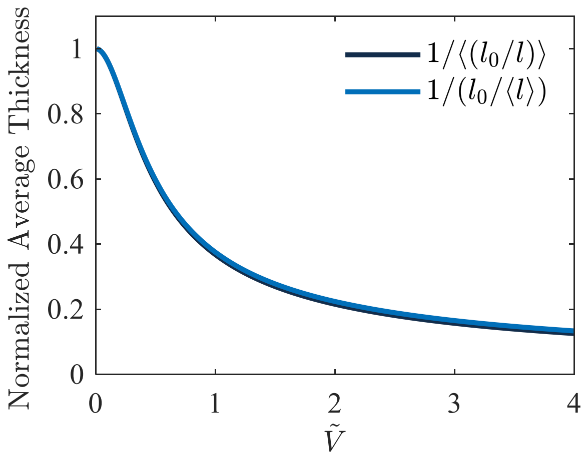

Fig. S1 Normalized average membrane thickness values predicted using two methods ($\frac{1}{\langle l_0/l \rangle}$: dark blue; $\frac{1}{l_0/\langle l \rangle}$: light blue) for bulging actuators as a function of the dimensionless membrane bulge volume $\tilde{V}$. Predicted values are very similar, with a slightly decreased thickness prediction for $\frac{1}{\langle l_0/l \rangle}$, at larger values of $\tilde{V}$ that correspond to greater membrane stretching.

To provide context for the thickness variation across a stretched membrane in comparison to the average membrane thickness (Eqn. (53)), we calculate membrane thickness distribution as shown in Fig. S2. This distribution is provided for an extreme case (standard geometery, highly stretched: $\overline{\lambda}$= 2.5, $\tilde{V}$= 3.5) and presented as the deviation from the average thickness $l_{\text{average}} = \langle l \rangle$. Under these conditions, there is a variation of ~ 1 μm in thickness across the membrane.

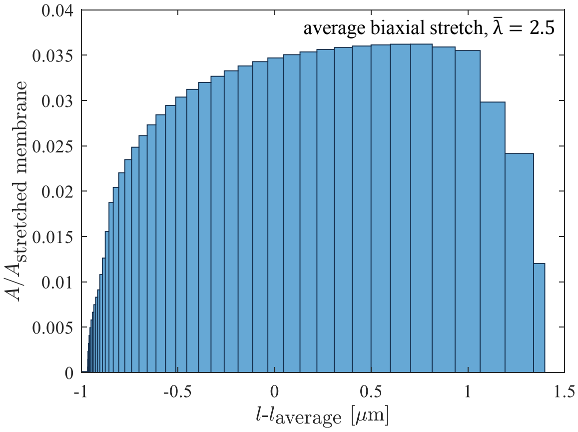

Fig. S2 The distribution of membrane thickness variation relative to the average membrane thickness, $l - l_{\text{average}}$ across the cross sectional area of the membrane. $\overline{\lambda} =$ 2.5. $\tilde{V} =$ 3.5. Standard geometry.

5.5 Determining the Hyperelastic Bulging Membrane's Average Biaxial Stretch

We determine the average biaxial stretch in the bulging membrane $\overline{\lambda}$ occurring across the membrane by integrating the biaxial stretch at each discretized ρ value, defined by

$$\lambda(\rho) = \sqrt{\lambda_\xi \lambda_\phi} = \sqrt{\frac{1}{\lambda_r}}, \tag{54}$$

where the average biaxial stretch across the entire membrane, is the expectation value determined by integrating the discretized biaxial stretch about the surface area of the membrane (subsection 5.3),

$$\overline{\lambda} = \langle \overline{\lambda} \rangle = \frac{2\pi a^2 \int_0^1 \sqrt{\frac{1}{\lambda_r}} \lambda_\xi \lambda_\phi \rho \; d\rho}{A}, \tag{55}$$

divided by the surface area A.

We compare this expectation value average biaxial stretch to an average using the evolution of surface area as given by

$$\overline{\lambda}_{\text{predicted}} = \sqrt{\frac{A}{A_0}}. \tag{56}$$

These two methods, are both plotted in Fig. S3 to compare the average biaxial stretch in the membrane $\overline{\lambda}$, determined using these methods. The expectation stretch quantity $\langle \overline{\lambda} \rangle$, predicts only a slightly increased biaxial stretch at increased membrane bulge volumes of $\tilde{V} \geq 1.5$. Therefore, for simplicity, and since biaxial stretch is provided only for increasing insight, we use $\sqrt{A/A_0}$ to define $\overline{\lambda}$.

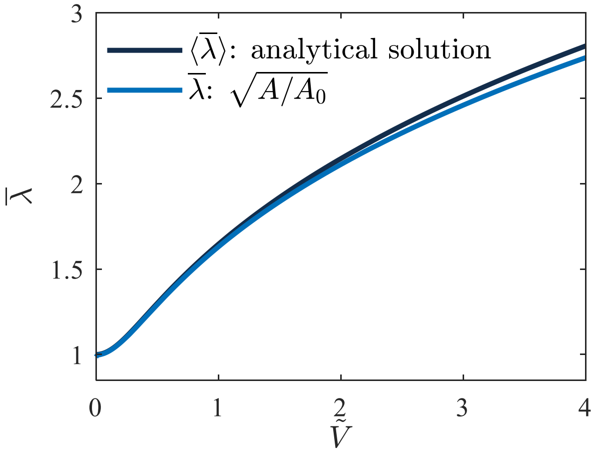

Fig. S3 Average biaxial membrane stretch is predicted using two methods ($\langle \overline{\lambda} \rangle$ (Eqn. 55: dark blue; $\frac{1}{l_0/\langle l \rangle}$ (Eqn. 56): light blue) for bulging actuators as a function of the dimensionless membrane bulge volume $\tilde{V}$. While both of these predictions exhibit similar behavior, $\langle \overline{\lambda} \rangle$ begins to show increased predictions at $\tilde{V} \geq 1.5$.

5.6 Determining Hyperelastic Bulging Membrane Turgor Pressure

Numerically integrating the bulging membrane deformation governing ODEs for a series of given dimensionless volume values $\tilde{V}$, yields a set of solutions, one of which is the applied dimensionless pressure necessary to produce that deformation. The dimensionless turgor pressure $\tilde{P}_t$ is defined as $\tilde{P}_t = \frac{P_t a}{C_1 l_0}$, meaning the turgor pressure with units of [Pa] is $P_t = \frac{\tilde{P}_t C_1 l_0}{a}$. We normalize the applied turgor pressure values by the membrane's Young's Modulus, resulting in $\frac{P_t}{E}$.

5.7 Determining the membrane pre-stretch

Solving this set of hyperelastic governing equations to determine the bulge deformation profile and turgor pressure, requires a set of boundary values, one of which is the initial geometry conditions of the membrane. It was seen throughout the imaging of the actuating chambers, that for all sets of chambers (geometries and materials), that the chambers were expanding slightly at the connection point with the membrane. To accurately capture the deformation profile resulting turgor pressure, we must set the appropriate pre-stretch ratio, $\lambda_{pre} = R(\tilde{V})/R_0$ as the boundary value for the initial membrane radial geometry stretch ratio. This means we set $\lambda_\phi = \lambda_{pre}$ at the membrane edge $\rho = 1$. This pre-stretch ratio is determined by using ImageJ to measure the radius of experimentally bulging actuator wells, and fitting a second order polynomial function with an intersection at $R/R_0 = 1$ to determine the prestretch ratio of chamber as a function of the dimensionless volume $\tilde{V}$. The resulting fit functions for all chamber geometries and materials are shown in Fig.S6.

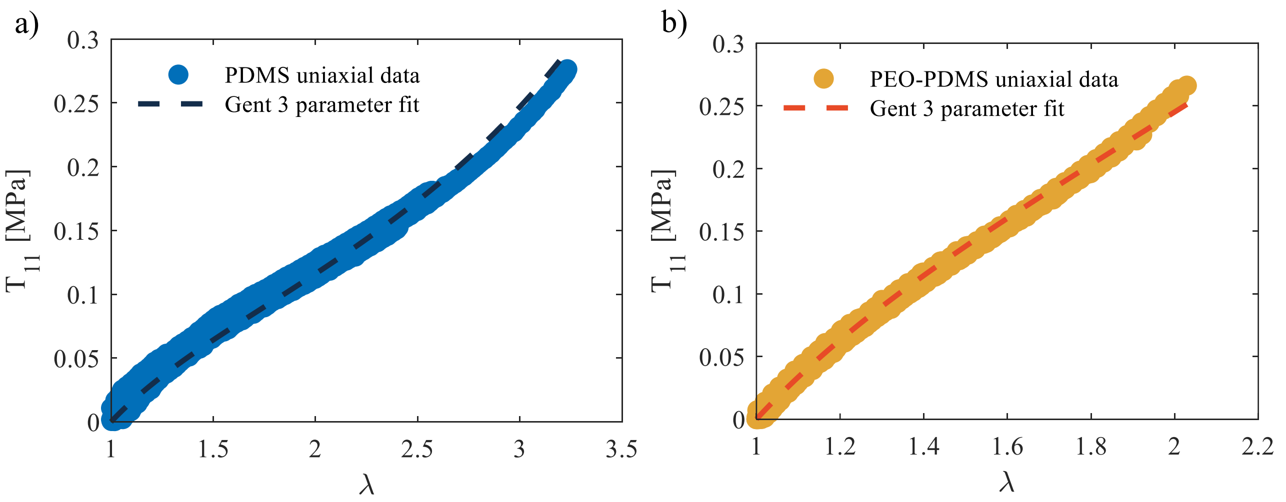

Fig. S4 Mechanical constitutive response behavior for PDMS and PEO-PDMS. (a) Engineering stress T_{11} versus stretch ratio λ for PDMS uniaxial tension test (blue circles), with Gent 3-parameter best fit response plotted (navy dashed line). (b) Engineering stress T_{11} versus stretch ratio λ for uniaxial tension test (gold circles) for PEO-PDMS, with Gent 3-parameter best fit response plotted (orange dashed line).

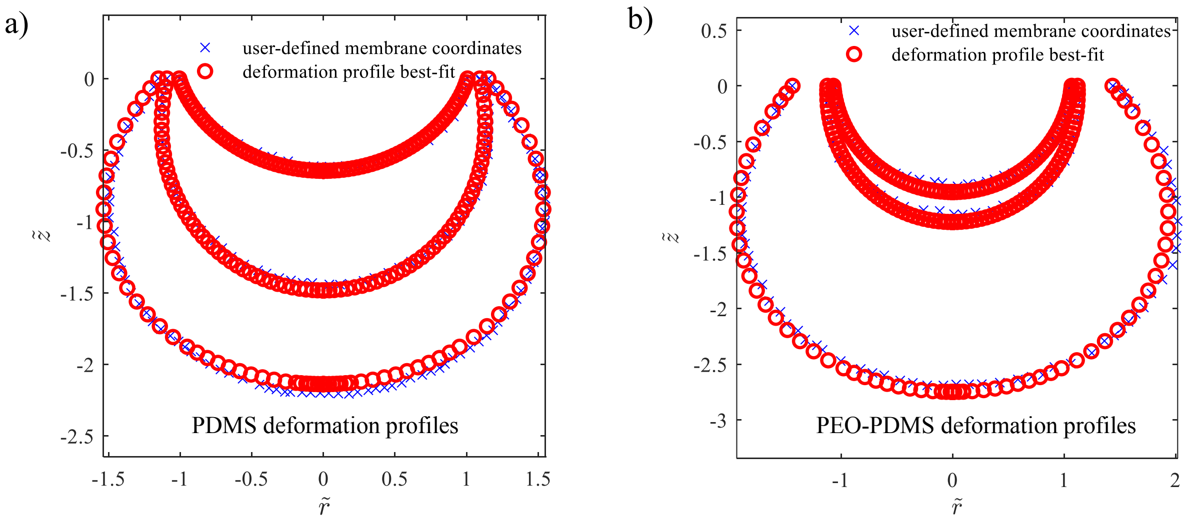

Fig. S5 Mechanical constitutive bulging behavior for PDMS and PEO-PDMS. (a) User-defined deformation profile points for 3 separate bulge volumes (blue x's) and resulting deformation profile best fit (red circles) for PDMS from Gent-3 parameter best fit material parameters. (b) User-defined deformation profile points for 3 separate bulge volumes (blue x's) and resulting deformation profile best fit (red circles) for PEO-PDMS from Gent-3 parameter best fit material parameters.

5.8 Hyperelastic Membrane Mechanics Parameters

The necessary membrane mechanics parameters: $f_A(\tilde{V})$, $f_l(\tilde{V}($, and $f_P(\tilde{V})$ are solved for by individually plotting $\frac{A}{A_0}$, $\frac{l}{l_0}$, and $\frac{P_t}{E}$ on a y-axis against $\tilde{V}$ on the x-axis. Using a spline-fit fit object function in MATLAB to reduce the computational cost of the fit algorithm, a resulting function for each of these three curves were determined per chamber and membrane geometry to solve for the hyperelastic membrane mechanics parameters.

6 Hyperelastic Data Analysis

We use two mechanical test geometries to capture the hyperelastic behavior of PDMS and PEO-PDMS, determining that the Gent 3-parameter model,[4] captures the response of both membrane materials, with different Gent constants for each. This information is used to model the mechanical response and turgor pressure gain of the membranes during deformation. The Gent 3-parameter strain energy density function is as follows,

$$W = -C_1 J_m \ln\left(1-\frac{J_1}{J_m}\right) + C_2 \ln\left(\frac{J_2+3}{3}\right),^{4} \tag{57}$$

with dependence on the first and second strain invariants J_1 and J_2, that are defined as follows,

$$J_1 = \lambda_1^2 + \lambda_2^2 + \frac{1}{\lambda_1\lambda_2}^{2} - 3, \tag{58}$$

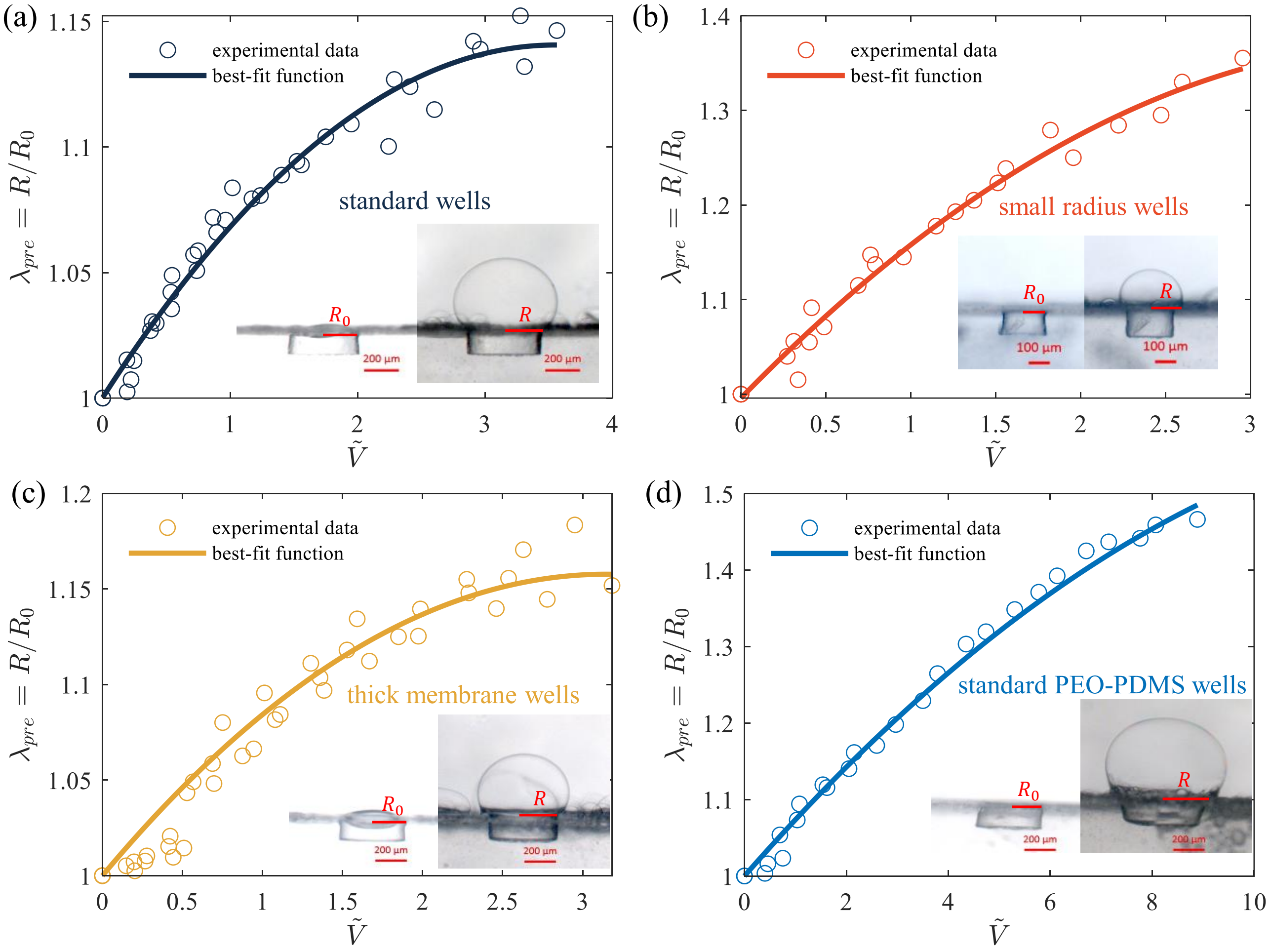

Fig. S6 Radial membrane pre-stretch effect (solid fit line) as a function of deformed bulge volume $\tilde{V}$, determined by fitting a second order polynomial to a set of experimental data (circles) for (a) standard PDMS wells, (b) small radius PDMS wells, (c) thick membrane PDMS wells, and (d) standard geometry PEO-PDMS well.

Table 1 Gent 3-parameter Model Material Constants

Material	C_1 (MPa)	C_2 (MPa)	J_m	E (Young's Modulus) (MPa)
PDMS	0.0316	0.0297	26	0.37
PEO-PDMS	0.0714	0.0536	45	0.75

$$J_2 = \lambda_1^{-2} + \lambda_2^{-2} + {\frac{1}{\lambda_1 \lambda_2}}^{-2} - 3, \tag{59}$$

and assumes incompressibility ($\lambda_1\lambda_2\lambda_3 = 1$), where λ_i is the stretch ratio in each of the three principal directions. Additionally, C_1, C_2 and J_m are materials constants that must be determined by fitting experimentally determined mechanical test data to nominal stress equations derived from this strain-energy density function. C_1 and C_2 are mechanical constants (each with units of [Pa]) that describe the shear modulus G behavior of the material,

$$G = 2(C_1 + C_2). \tag{60}$$

The nominal or engineering stress relation for uniaxial tension, $T_{11,\text{uniaxial}}$, is dependent on the principal stretch ratio along the axis of the applied tension, which is described as $\lambda_1 = \lambda$. Employing the assumption of incompressibility and the uniaxial geometry, the two other principal stretch ratios are given by $\lambda_2 = \lambda_3 = \lambda^{-1/2}$ such that

$$T_{11,\text{uniaxial}} = \frac{1}{\lambda}\left(\frac{C_1 J_m \lambda^2}{J_m - J_1} - \frac{2C_2\lambda^{-2}}{J_2 + 3} - 2(C_1 - \frac{C_2}{3})\right). \tag{61}$$

Simultaneously fitting the uniaxial test data (Fig. S4), and user defined points on three membrane deformation profiles (Fig. S5) to their respective deformation equations derived from Eqn. 57 using nonlinear least square regression in MATLAB, we solve for C_1, C_2 and J_m for both PDMS and PEO-PDMS. The resulting fits are shown in Fig. S4 (the uniaxial response), and Fig. S5 (the fit to user-defined deformation profiles). The material constants are summarized in Table 1. Additionally, we can determine the Young's Modulus E, of each material with these constants using G (Eqn. 60) and the incompressibility assumption,

$$E = 3G. \tag{62}$$

Utilizing the 3 fit parameters as explained above, we find the Young's modulus E, of PDMS and PEO-PDMS are 0.37 MPa and 0.75 MPa, respectively.

7 Determining Bulging Membrane Permeability

We discuss the methods of solving for both stretch-independent and stretch-dependent permeability. Here we provide additional details on these methods and results.

7.1 Constant Linear Elastic Permeability fit

As discussed in the paper, we simultaneously fit experimental PDMS actuation data to the model with linear elastic membrane mechanics parameters, solving for a constant permeability value as the fit parameter. As linear elasticity is only valid for small deflections, we fit this model to actuation data where the biaxial stretch, $\overline{\lambda} \leq 1.4$, which corresponds to volume ratio data $V/V_0 \leq 1.3$. The resulting permeability fit parameter is 2.02×10^{-12} $[\frac{m^2}{s}]$, which is shown in Fig. S7b, and fits the initial small deflection response, but after the linear elastic volume ratio regime, this fit overestimates the response. This permeability value is used to determine the mobility value (Eqn. 26), and then the resulting time constant ($\tau = -\frac{l_0 V_0}{L \Pi_0 A_0}$) for the given chamber configuration that is being used. When the experimental time is nondimensionalized by the chamber's respective time constant τ, the resulting volume ratio actuation behavior collapses in this linear elastic regime for all PDMS chamber configurations, when plotted in dimensionless time $\tilde{t}$, as seen in Fig. S7a.

7.2 Constant Permeability fit

The constant P_w hyperelastic fit discussed in the paper, shows the fit in comparison to the reference chamber conditions ($a = 200$ μm, $l_0 = 20$ μm, $C_0 = 3$ M). Using a nonlinear least-squares regression in MATLAB, we solve for a best-fit permeability of 8.35×10^{-13} $[\frac{m^2}{s}]$. Utilizing this permeability value in our model, the actuation data compared to the theory curve for all PDMS membrane chambers (small radius chamber: $a = 100$ μm, thick membrane chamber: $l_0 = 26$ μm, and reduced osmotic loading: $C_0 = 3$ M) are shown in Fig. S8. This fit parameter captures the middle-time response and high-stretch response behavior of the reference chamber, small radius chamber, thick membrane chamber, and reduced osmotic loading chamber better than the linear fit at large membrane stretch values (later stage actuation). However, it underestimates the initial rate of actuation for these chambers.

7.3 Solving for Stretch Dependent Permeability

We solve for stretch-dependent permeability by isolating the mobility term (and therefore permeability), using the following equation:

$$L(\tilde{V}) = \frac{P_w C_w}{RT}\frac{V_m M_W}{\rho} = -\frac{d\frac{V}{V_0}}{dt}\frac{l_0 V_0}{A_0 \Pi_0}\frac{1}{f_A(\tilde{V}) f_l(\tilde{V})}\frac{1}{\left(\frac{1}{\frac{V}{V_0}} + \frac{E f_p(\tilde{V})}{\Pi_0}\right)} \tag{63}$$

To determine an instantaneous value of mobility L, an instantaneous value of the volumetric flow rate $\frac{dV/V_0}{dt}$ is necessary. We determine a series of instantaneous volume flow rates, by create overlapped time-bins within our data, and using a linear fit function within MATLAB to fit overlapping piece-wise functions to actuation rate data. The resulting slope at each piece-wise linear fit is taken as the instantaneous flow rate $\frac{dV/V_0}{dt}$ at the mid-point time of that binned region. An example of the resulting piecewise fits (dark blue line segments) plotted against the actuation data (dark blue circles) for the reference chamber ($a = 200$ μm, $l_0 = 20$ μm, $C_0 = 3$ M), is shown in Fig. S9.

7.4 Thickness-dependent permeability

As described in the main text, previous studies by Firpo et. al[5] determined a critical length scale L_c at which the surface reactions can become highly nonequilibrium and below which the permeability decreases with decreasing membrane thickness. However, membrane thickness in the deformed state is not uniform, as shown in Fig. S2. To quantify the sensitivity of the thickness dependence to these small thickness changes, we plot the highest and lowest L_c predictions from Fig. 6a, $L_c = 10$ μm and $L_c = 200$ μm, but for a differential membrane thickness, $l - l$, where l is ± 1 μm. Between these differential values, we shade in the regions on Fig. S10 to provide approximate sensitivity analysis of the Firpo thickness-dependence to small thickness changes. The results support our interpretation within the main text.

8 Thin Film Deformation

At high levels of membrane stretching, $\overline{\lambda} = \sqrt{A/A_0} \geq 3.5$, the bulging membranes on the microactuators begin to exhibit color gradients, with the most concentrated color appearing at the maximum deflection in the center of the membrane. Intriguingly, color tends to fall within the blue/violet color spectrum (shown in Fig. S11(a-b)) initially, increasing to warmer colors as the membrane continues to stretch. We hypothesize that these colors appear as the thin film deforms to thicknesses approaching a length-scale close to the wavelength of visible light. Order of magnitude estimations of the film thickness in the region of maximum deflection support this hypothesis (This region has the smallest thickness.) (Fig. S11c).

We obtain film thickness estimates from a combination of experimental observation, finite element calculation, and a few simple geometric relationships. The dimensionless membrane volumes in Fig. S11 (a-b) correspond to $\tilde{V} = 9$ (a) and $\tilde{V} = 10$ (b). We measure the experimental surface area A of these membranes at each of the observed $\tilde{V}$ and estimate the experimental average thickness of these membranes ($l_{\text{exp:average}}$) using the following relationship, assuming incompressibility of the PDMS membrane,

$$l_{\text{average}}(\tilde{V}) = \frac{V_{\text{membrane}}}{A(\tilde{V})} \tag{64}$$

where V_{membrane} is the initial cylindrical membrane volume, defined by a radius of $a = 200$ μm and initial thickness of $l_0 = 20$ μm. The average thickness estimates using this method range from 1.5-1.66 μm, as described in Table 2. In validation,

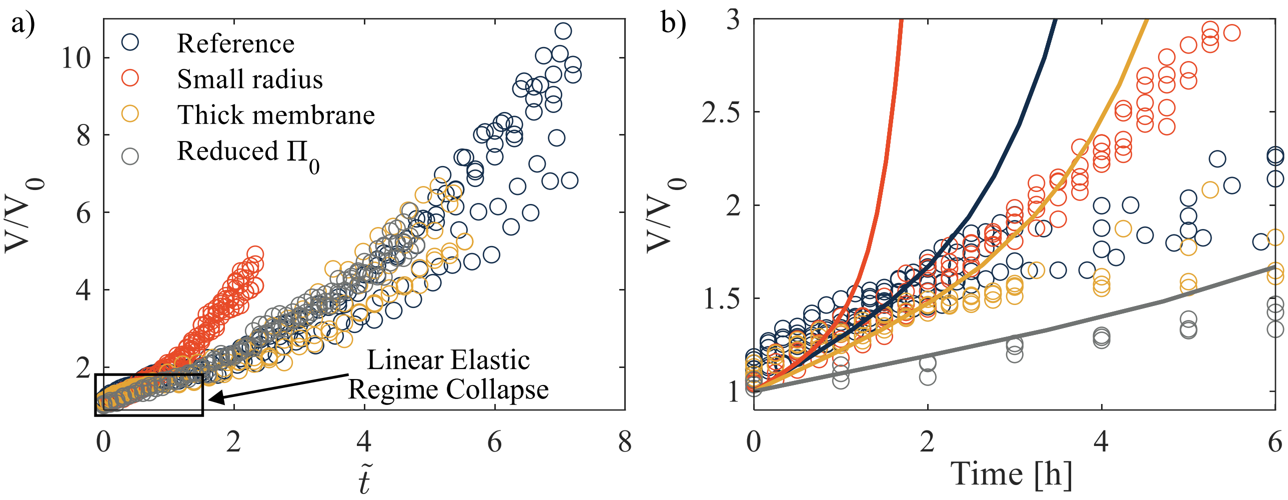

Fig. S7 Linear elastic constant permeability fit. (a) The collapse of all experimental data in the linear elastic regime occurs, when plotted in dimensionless time. (b) The respective best-fit volumetric chamber evolution model employing linear elastic membrane mechanics parameters plotted in experimental time [h], fits each individual experimental chamber configuration, but only in the linear elastic regime ($\frac{V}{V_0} \leq 1.3$).

Table 2 Thin Film Bulging Thickness

$\tilde{V}$	experimental: $l_{average}(\tilde{V})$ (μm)	prediction: $l_{average}(\tilde{V})$ (μm)	estimated thickness at max. deflection (nm)
9	1.66	1.34	880
10	1.50	1.23	800

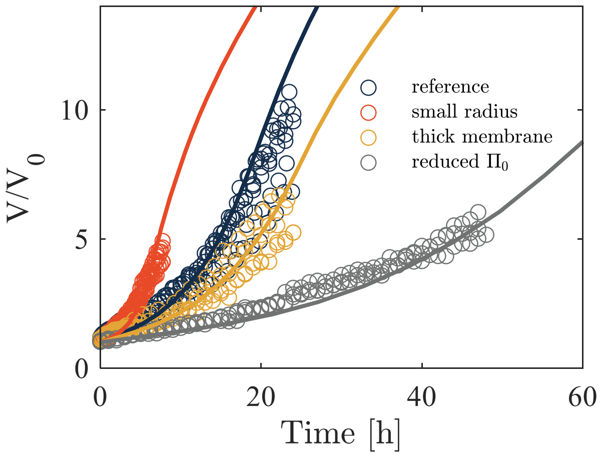

Fig. S8 Constant permeability fit for a hyperelastic membrane shown against experimental actuation. A best fit water permeability P_w is found using nonlinear least-squares regression for all actuation data and utilized in theory to show predictive actuation behavior of a hyperelastic membrane exhibiting constant P_w.

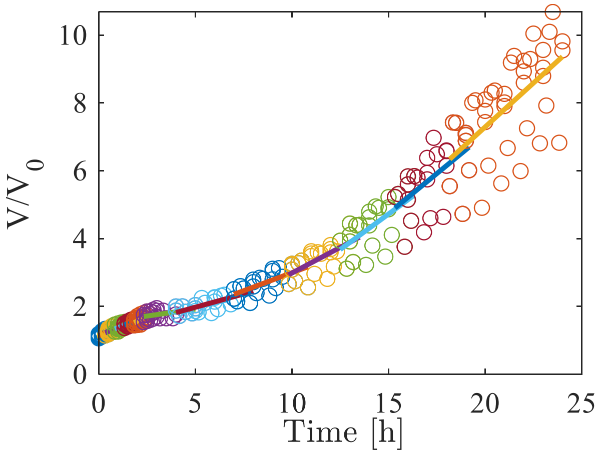

Fig. S9 Piece-wise fits to each small time-binned region of the $\frac{V}{V_0}$ curve, where the slope of each piece-wise linear-function corresponds to the instantaneous volumetric flow rate $\frac{dV/V_0}{dt}$ of each region.

we check these measurements against the average thickness predicted using the constitutive model description of the nonlinear bulge, specifically the inverse of function $f_l(\tilde{V})$. Both values are in agreement as shown in Table 2 with estimates on the same order of magnitude, further demonstrating the consistency of the model in capturing the membrane behavior. Both of these methods (experimental measurement and predictive model) provide average film thicknesses, however the color appearing in the film is concentrated to specific regions, mainly the region at the maximum membrane deflection. This is due to the fact that greater film stretching occurs at the maximum deflection as illustrated by Fig. S11(c). The curves in this figure arise directly from the solutions to the membrane deflection and thickness calculations. Due to incompressibility, the transverse stretch ratio λ_r is the inverse of the product of the longitudinal and latitudinal stretch ratios (λ_ξ, λ_ϕ), and when multiplied by the initial membrane thickness l_0, the stretch dependent membrane thickness along the membrane profile, $l(\rho)$, is defined as

$$l(\rho) = \lambda_r(\rho) l_0. \tag{65}$$

The thickness of the membrane at the membrane's center where

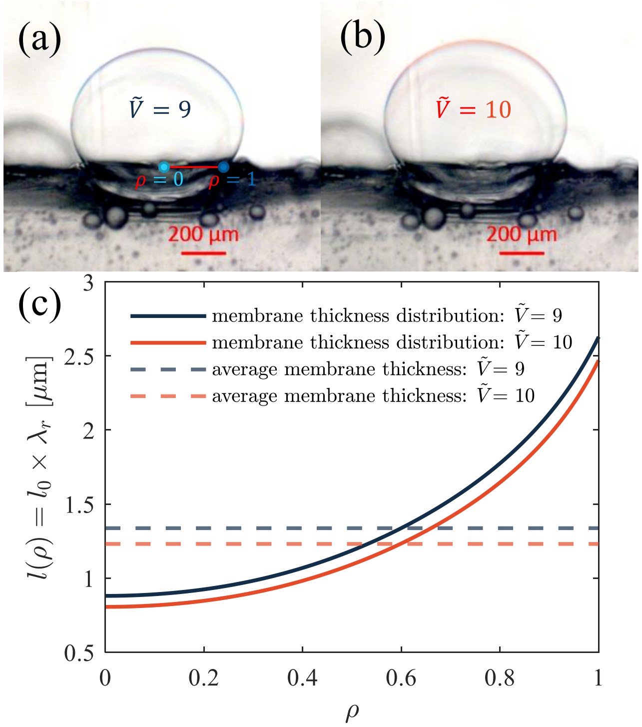

Fig. S11 Thin films deforming on PDMS devices fabricated using the (a-b) reference configuration. At these high levels of deformation [$\tilde{V} = 9$ (a), and $\tilde{V} = 10$ (b)] the bulging membranes begin to exhibit color at the point of maximum deflection. As the membrane experiences greater stretch the color evolves (a: violet color at maximum, b: orange color at maximum). (c) The membrane thickness distribution is non-uniform shown by the solid curves ($\tilde{V} = 9$: blue, $\tilde{V} = 10$: orange), with the thinnest region, occurring at the membrane's center where maximum deflection occurs. This is compared to the average membrane thickness in the entire membrane (dashed line), where the maximum stretch is 34% less than the average stretch.

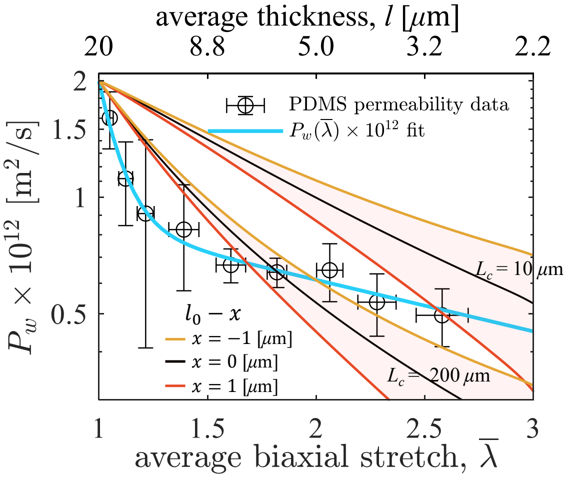

Fig. S10 Deformation-mediated permeability P_w of PDMS where instantaneous permeability (black circles), averaged from all four PDMS chamber conditions, as a function of average biaxial membrane stretch $\bar{\lambda}$ (lower x-axis) and corresponding stretch dependent $P_w(\bar{\lambda})$ fit teal. This permeability-fit is compared to thickness-dependent (l, upper x-axis) permeability model. Shaded regions (light red) bound curves describing L_c at values of (L_c= 10, 200 μm) with ± 1 μm thickness bounds.

the maximum deflection occurs is at a value of $\rho = 0$. The average membrane thickness is defined by the average thickness $1/\langle l_0/l \rangle$ determined from $f_l(\tilde{V})$, multiplied by the initial membrane thickness l_0

$$l_{\text{average}} = l_0 \frac{1}{\langle l_0/l \rangle}. \tag{66}$$

These average thickness values are plotted in Fig. S11c with dashed lines. The membrane thickness at the center point predict the minimum film thickness (as opposed to using the average film thickness). For both $\tilde{V} = 9$ and $\tilde{V} = 10$, the minimum membrane thickness (which occurs at the maximum deflection) is approximately 34% less than the average membrane thickness. Therefore, the membrane thickness at the maximum deflection (the region where we see concentrated color) for the $\tilde{V} = 9$ and $\tilde{V} = 10$ actuated bulges are approximately 880 nm and 800 nm, respectively. Both values have an order of magnitude similar to that of the wavelength of visible light (400-700 nm).

Notes and references

1 R. Gavara and V. Compan, *JOURNAL OF BIOMEDICAL MATERIALS RESEARCH B: APPLIED BIOMATERIALS*, 2017, **105**, 2218–2231.

2 S. Timoshenko and S. Woinowsky-Krieger, *Theory of plates and shells*, McGraw-Hill, 1959, p. 580.

3 J. J. Vlassak and W. D. Nix, *J. Mater. Res*, 1992, **7**, 3242–3249.

4 A. N. Gent, *International Journal of Non-Linear Mechanics*, 2005, **40**, 165–175.

5 G. Firpo, E. Angeli, L. Repetto and U. Valbusa, *Journal of Membrane Science*, 2015, **481**, 1–8.